A Climatology of Strong Large-Scale Ocean Evaporation Events. Part II: Relevance for the Deuterium Excess Signature of the Evaporation Flux

FRANZISKA AEMISEGGER

Centre for Environmental and Climate Research, Lund University, Lund, Sweden, and Institute for Atmospheric and Climate Science, ETH Zurich, Zurich, Switzerland

JESPER SJOLTE

Department of Geology Quaternary Science, Lund University, Lund, Sweden

(Manuscript received 31 August 2017, in final form 25 May 2018)

ABSTRACT

This paper discusses the relevance of transient events of strong large-scale ocean evaporation (SLOE) for the deuterium excess of marine boundary layer vapor d using a theoretical framework that invokes the closure assumption. We argue that during SLOE events, d is essentially determined by the evaporation flux signature. Distinct high d during SLOE with global-mean values in the range of 12‰–23‰ depending on the nonequilibrium fractionation factor α_k result from the large air–sea humidity gradients reflected in low relative humidity with respect to sea surface temperature (h_s = 53% ± 9%) that characterize these events. Extratropical cyclones are highlighted as an important driver for the variability of d. On the one hand, they are themselves associated with high h_s and low d, especially in areas of cloud formation and precipitation in the warm sector. On the other hand, cyclones are the main driver inducing SLOE events with high d in regions of cold-air advection upstream of their path. The sensitivity of d to its direct climate controls (h_s and SST) is analyzed during SLOE for different α_k formulations and found to be coherent with d–h_s and d–SST slopes determined from available observations. The d–h_s relationship exhibits a robust negative correlation as opposed to the d–SST relationship, which shows regional and time-scale-dependent variations in strength and sign that are induced by indirect h_s–SST cross-correlation effects. The dynamical features involved in SLOE generation appear to exert a key control on the moisture source properties relevant for d in the extratropics.

1. Introduction

Events of strong large-scale ocean evaporation (SLOE) in the mid-to-high latitudes (>30° in the Northern and Southern Hemispheres) have been shown by Aemisegger and Papritz (2018, hereinafter Part I) to be induced by cold and dry airstreams. Such events are found to be particularly frequent in wintertime over the warm ocean western boundary currents (WBCs) as well as along the sea ice edge. The spatial occurrence frequency patterns of SLOE highlights several regions that have previously been identified as footprint areas of Greenland and Antarctic precipitation (Delaygue et al. 2000; Werner et al. 2001; Noone and Simmonds 2002; Sodemann et al. 2008a; Sodemann and Stohl 2009). By construction, SLOE events strongly influence the isotopic composition of low-level atmospheric water vapor as they are defined using a criterion of high atmospheric moisture uptake efficiency (i.e., conditions in which the ocean evaporation flux is large compared to the near-surface water vapor content). The second-order isotope variable deuterium excess d (Dansgaard 1964) is a particularly interesting tracer for moisture source conditions, because it is sensitive to nonequilibrium conditions occurring in unsaturated environments. It is defined as follows:

$$d = \delta^2\mathrm{H} - 8\delta^{18}\mathrm{O}, \tag{1}$$

with δ^2H and δ^{18}O following the commonly used δ notation for water isotopes, which expresses the relative deviation of the isotopic mixing ratios R from the internationally accepted primary water isotope

Corresponding author: Franziska Aemisegger, franziska.aemisegger@env.ethz.ch

DOI: 10.1175/JCLI-D-17-0592.1

standard, the Vienna mean standard ocean water (VSMOW2; Coplen 2011),

$$\delta = \frac{R - R_{\mathrm{VSMOW2}}}{R_{\mathrm{VSMOW2}}}, \tag{2}$$

with $R^{2_{\mathrm{H}}}_{\mathrm{VSMOW2}} = 155.76 \times 10^{-6}$ and $R^{18_{\mathrm{O}}}_{\mathrm{VSMOW2}} = 2005.2 \times 10^{-6}$ (with δ generally expressed in ‰).

To first order, d is conserved during transport and moderate rain out along an air parcel's trajectory (Petit et al. 1991; Ciais and Jouzel 1994). The d has thus been the focus of early isotope studies beginning in the 1960s that sought to understand the relationship between stable water isotopes and air–sea variables at the moisture source (Dansgaard 1964; Craig and Gordon 1965; Merlivat and Jouzel 1979, hereinafter MJ79). Thereafter, many studies have linked d in Greenland and Antarctic ice cores to past changes in source conditions and/or source locations due to changes in circulation patterns (Jouzel et al. 1982; Johnsen et al. 1989; Vimeux et al. 1999; Stenni et al. 2001; Noone and Simmonds 2004; Masson-Delmotte et al. 2005; Jouzel et al. 2007a; Steffensen et al. 2008; Markle et al. 2017).

SLOE events are expected to be associated with a distinct d signature in marine boundary layer water vapor that is different from normal conditions. The primary aims of this study are to characterize the typical d signature of SLOE events and to investigate its sensitivity to the variability in air–sea variables at the moisture source in a climatological sense. Additionally, in view of their important role in the generation of SLOE, the influence of extratropical cyclones on the variability of d will be discussed.

The Craig and Gordon model (Craig and Gordon 1965, hereinafter CG65; see also section 2b) has become the cornerstone of isotopic studies focusing on the isotope effects associated with the evaporation of ocean water since its introduction in 1965. This model predicts the isotopic composition of the evaporation flux as a function of environmental state variables and isotope fractionation factors. The three main environmental controls in the CG65 model are the ratio of the specific humidity of the air and the saturation specific humidity at sea surface temperature (relative humidity normalized to sea surface temperature h_s), the sea surface temperature (SST), and the near-surface wind speed.

The strong physical link predicted by the CG65 model between h_s and the isotope signature of boundary layer water vapor, and in particular d_v, has been supported by recent measurements over the ocean (e.g., Gat et al. 2003; Uemura et al. 2008; Kurita 2011; Steen-Larsen et al. 2014; Benetti et al. 2014) and over land (Angert et al. 2008; Pfahl and Wernli 2008; Welp et al. 2012; Aemisegger et al. 2014), when the ambient moisture is predominantly originating from ocean evaporation. These studies show that at synoptic time scales d_v is strongly correlated with h_s. Furthermore, as noted by Pfahl and Sodemann (2014), the d_v–h_s relationship emerging from different recent measurement campaigns are linear and very similar despite the great variety of the geographical locations and conditions in which these measurements were performed. The similarity of the identified d_v–h_s relationship from measurements from different oceanic regions suggests that d_v might be mainly determined by the fresh ocean evaporate's d_e signature and that the background d_v signature of the advected airstreams is of secondary importance. This would confirm the validity of the closure assumption for d that has been proposed by MJ79. The closure assumption states that the only source of low-level atmospheric water vapor over the ocean is ocean evaporation and the only sink is transport into the free troposphere (MJ79). The effects of horizontal advection, precipitation evaporation, and subsidence and thus the potential feedback of ambient d_v on d_e are thus neglected. In this study, we use the closure assumption and apply it to the CG65 formulation, yielding the CG65closure model as proposed by MJ79 (see also section 2c) to globally estimate d_c during SLOE events. Arguments for why d_c is a good estimate of d_e during SLOE events are presented and discussed in section 2c.

Applying the closure assumption simplifies the calculation of d_e but neglects the feedback of the isotope signature of ambient air on the ocean evaporate. As a result, the validity of the closure assumption at the local scale and over short time scales has been critically discussed in the past, in a study based on model data from an isotope-enabled global numerical climate model (herein abbreviated as isoGCM; Jouzel and Koster 1996). However, the sensitivity of the simulated d_v by isoGCMs to the environmental conditions at the moisture source does not reflect the sensitivities obtained from empirical data. Risi et al. (2013) showed that the slope of the d_v–h_s relationship was strongly underestimated in the isotope-enabled Laboratoire de Météorologie Dynamique zoom model (LMDZiso) isoGCM for a simulation over the Southern Ocean compared to measurements from the ship campaign presented in Uemura et al. (2008). The reasons for this underestimation as well as the relatively large biases of simulated d_v that are also seen in other models (Jouzel et al. 2007b; Yoshimura et al. 2008; Steen-Larsen et al. 2017) have not yet been identified. The closure assumption thus allows us to investigate the environmental controls on d_c based on observationally well-constrained reanalysis data and within a simpler framework, than if

an isoGCM is used. In this way, our study contributes to a physically based description of the mechanisms leading to the observed sensitivities of d_v to air–sea variables. This is a necessary step in the pursuit of gaining a better understanding of the proxy information available from d at different time scales.

Even though h_s is the direct physical controlling factor of d_e at the time scale at which evaporation occurs, as reflected by recent d_v measurements, the assumption that over long glacial–interglacial time-scale changes in global-mean h_s over the ocean are small [see Schneider et al. (2010) for a physically based discussion and justification of this assumption] has led many studies of d in Antarctic ice cores to interpret these signals as a moisture source SST signal (e.g., Vimeux et al. 1999; Stenni et al. 2001). This assumption has been questioned by Pfahl and Sodemann (2014), who argue that the interpretation of d variations in paleorecords should be adapted to reflect climatic influences on h_s during evaporation. Indeed, even if the global-mean surface relative humidity changes are strongly constrained by the surface energy balance and remain small over long time scales, local changes in moisture source h_s may affect the d_v signature. Such changes in moisture source h_s can, for example, be due to shifts in the storm tracks (Shaw et al. 2016) and frontal activity (Rudeva and Simmonds 2015) or the location and extent of the warm ocean WBCs both affecting the frequencies and spatial distribution of SLOE and the geographical location of moisture sources associated with a certain ice core drill site. Our hypothesis is that the discrepancies between the interpretation of moisture source d_v as a proxy for h_s at short time scales and a proxy for SST at longer time scales arises as a result of the changing cross-correlation patterns between these two variables, when going from synoptic to interannual variability regimes. This hypothesis is tested in the present study using the SLOE framework.

In this paper, we will thus investigate the phase space of the climate controls on moisture source d_c during SLOE events at different time scales. After shortly introducing the dataset used and the analysis methods in section 2a, we critically discuss the assumption involved in predicting d_c solely from reanalysis data (sections 2b and 2c). We show that within the framework of the CG65 model, the closure assumption of MJ79 is relatively good at low h_s such as is typically observed during SLOE. Thereafter, we discuss the global patterns of winter mean d_c during SLOE using different parameterizations of the nonequilibrium fractionation factor α_k and compare the results to latent heat flux weighted seasonal means (section 3a). Then, the importance of h_s and SST as controlling factors of d_c at different time scales is analyzed and the nature of the indirect effects of the h_s–SST cross correlation is investigated. Subsequently, the role of the wind speed is discussed briefly (section 3b). The slopes of the linearized d_c(SST) and $d_c(h_s)$ relations for the different parameterizations are then compared to available estimates from different measurement studies (section 3d). Finally, a synthesis on the use of different α_k is made (section 3e) and conclusions are drawn (section 4).

2. Data, theory, and methods

a. Dataset and relevant meteorological fields

The climatology of d_c in a near-surface oceanic environment and its climate controls presented here is based on 6-hourly global ERA-Interim data (Dee et al. 2011) from the European Centre for Medium-Range Weather Forecasts (ECMWF) during the period 1979–2014. The main motivation for the use of this dataset is its global coverage, 6-hourly temporal resolution, and good quality. The meteorological fields used from the ERA-Interim dataset are interpolated from a T255 spectral resolution to a regular horizontal grid of 1° resolution with 60 vertical levels. Three main climate variables are used in this study: h_s, SST, and 10-m wind speeds $|U|^{10\,\mathrm{m}}$. A more detailed discussion on the reanalysis data product quality and the objective identification method of SLOE events can be found in Part I.

Near-surface ocean regions affected by extratropical cyclones are identified using a slightly updated version (Sprenger et al. 2017) of the algorithm of Wernli and Schwierz (2006). Regions within closed sea level pressure (SLP) contours that contain one or several local sea level pressure minima are defined as cyclone masks. The maximum length of the outermost pressure contour is restricted to 7500 km. Using a conservative method of association between cyclone features and SLOE objects, SLOE is found to be frequently linked to extratropical cyclones (>70% for the North Atlantic; Part I).

Composites of d_c during SLOE and cyclone passages, respectively, are computed from 6-hourly fields taking only values into account that are affected by the respective feature. In section 3 below we will focus on winter mean composites, because both SLOE and cyclone frequencies are highest during this season, thus making the composite estimate the most robust. Seasonal mean estimates of surface latent heat flux (SLH)-weighted d_c are also computed to compare the SLOE and cyclone composites to a reference d_c estimate from the reanalysis data. This SLH-weighted mean (for $\mathrm{SLH} \leq 0\,\mathrm{W\,m^{-2}}$, flux from the ocean to the atmosphere) d_c is an estimate of d_c during evaporation in general, not only selected for strong evaporation.

To assess the influence of the moisture source conditions and in particular h_s and SST on d_c, Pearson correlation coefficients are computed at monthly and interannual time scales from SLOE composites. No detrending or removal of the annual cycle is performed, since the drivers behind the annual cycle on the one hand and the interannual variability on the other hand are of interest here. We apply orthogonal univariate linear least squares regressions to determine the sensitivity of d_c to its climate controls. Note that our analysis is limited by the fact that we only look at linear cross relationships among d_c, h_s, and SST. To first order, we expect a close to linear relationship between h_s and d_c, as well as between SST and d_c, as discussed in sections 2b and 2c, which justifies the use of Pearson correlation coefficients and linear regression analysis to characterize these relationships.

To compute d_c from the ERA-Interim dataset we use the closure assumption from MJ79 and apply it to the CG65 model. In the following, we will first discuss the influence of the relevant environmental conditions controlling d_e in the formulation of the CG65 model from a theoretical perspective without the closure assumption (section 2b) and then assess the impact of the closure assumption (section 2c).

b. *The CG65 model*

The isotope ratio of the evaporation flux following Craig and Gordon (1965) is

$$R_e = \frac{\frac{R_\ell}{\alpha} - h_s R_v}{\alpha_k (1 - h_s)} \tag{3}$$

where $\alpha = R_\ell / R_v$ is the temperature-dependent equilibrium fractionation factor relating the isotope ratio of the liquid ocean-surface R_ℓ to the isotope ratio of the vapor-phase R_v, with α_k the nonequilibrium fractionation factor resulting from differences in the diffusivity of the different isotopes.

Three different formulations of α_k are used, which can all be expressed based on the diffusion coefficients of water isotopes of Merlivat (1978) (see section 3e):

1) α_k(MJ79), with wind-dependent factors of MJ79 based on the water evaporation model for rough ($|U|^{10\,\mathrm{m}} \geq 7\,\mathrm{m\,s^{-1}}$) and smooth ($|U|^{10\,\mathrm{m}} < 7\,\mathrm{m\,s^{-1}}$) surfaces by Brutsaert (1975);
2) α_k(PW09), with wind-independent factors of Pfahl and Wernli (2009, hereinafter PW09); and
3) α_k(MJ79cstu6ms), with wind-independent factors using α_k as obtained from the wind-dependent factors of MJ79 for $|U|^{10\,\mathrm{m}} = 6\,\mathrm{m\,s^{-1}}$ (MJ79cstu6ms). This $|U|^{10\,\mathrm{m}}$ value is chosen because it is close to the mean $|U|^{10\,\mathrm{m}}$ of $9\,\mathrm{m\,s^{-1}}$ during strong ocean evaporation (Part I) but still in the smooth evaporation regime. The currently available observations generally follow the $d_c(h_s)$ dependency as predicted by closure in the smooth regime and rarely show weaker sensitivities of d_v to h_s as predicted with α_k(MJ79) in the rough regime (e.g., PW09; Benetti et al. 2014; Steen-Larsen et al. 2014, 2015).

The phase space describing the variability of d_e is spanned by h_s, SST, d_v, and therewith $|U|^{10\,\mathrm{m}}$, when using α_k(MJ79) as illustrated in Fig. 1a, in which the colored shading is shown as a function of h_s and d_v. Figure 1a was obtained by simulating all possible combinations of h_s and R_v using Eq. (3) and assuming SST = 20°C and $|U|^{10\,\mathrm{m}} = 6\,\mathrm{m\,s^{-1}}$. The pattern shown in Fig. 1a is shifted vertically for changing SST conditions and tilted for changes in $|U|^{10\,\mathrm{m}}$. The impact of the different controlling factors and the implications of the closure assumption on d_e will be discussed in the next section with the help of Fig. 1a.

c. *The closure assumption of MJ79 and its impact on d_e estimates*

The use of the closure assumption of MJ79 simplifies the quantitative description of d_e such that it can be calculated from h_s, SST, the molecular diffusivities of the isotope compounds in air, and wind-speed conditions only, without including the feedback from d_v. In this section we argue that the isotope signature of low-level moisture during a SLOE event is mainly determined by local evaporation. The chosen identification method of SLOE ensures that the identified evaporation features contribute substantially to the locally available near-surface humidity. Thus, a SLOE event as defined here has a strong impact on the isotope signature of low-level moisture and the conditions associated with such events warrant the use of the closure assumption. The isotopic ratio of the evaporation flux R_e in this case equals the isotopic ratio of boundary layer water vapor R_v (MJ79):

$$R_e = R_v = R_c, \tag{4}$$

with R_e the isotope ratio of ocean evaporation, R_v the isotope ratio of ambient water vapor, and R_c the isotope ratio as obtained from CG65closure [see Eq. (5) below].

If the closure assumption [Eq. (4)] is applied, Eq. (3) simplifies to the following formulation introduced by MJ79 (herein the CG65closure):

$$R_c = \frac{R_\ell}{\alpha[\alpha_k + h_s(1 - \alpha_k)]}. \tag{5}$$

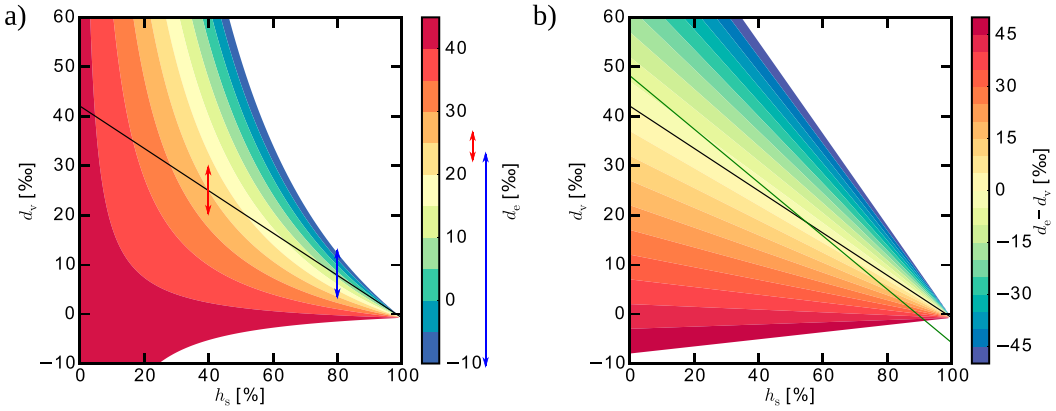

FIG. 1. (a) Deuterium excess in ocean evaporation d_e (colored shading) and (b) deviation from closure $\Delta d_{e-v} = d_e - d_v$ (colored shading) as a function of h_s and d_v for SST = 20°C and the nonequilibrium fractionation factors α_k from MJ79 with $|U|^{10\,\mathrm{m}} = 6\,\mathrm{m\,s^{-1}}$. The black solid line illustrates the closure assumption where $d_v = d_e$. Note that a flatter structure (contour lines and black closure line) would be obtained if using nonequilibrium factors from MJ79 and a $|U|^{10\,\mathrm{m}}$ of 7.1–12 $\mathrm{m\,s^{-1}}$. Also, $|U|^{10\,\mathrm{m}}$ has a tilting effect on the represented pattern depending on the chosen α_k formulation. Variations in SST induce a vertical displacement in d_v and a shift in the color range of d_e. The shifts induced by SST are toward higher d_e values for higher SSTs. The green line in (b) shows the empirical $|U|^{10\,\mathrm{m}}$ and SST-independent $d_e(h_s)$ relation from Pfahl and Sodemann (2014). The red and blue arrows on the color bar in (a) illustrate the range of possible d_e values for a 10‰ range in d_v at $h_s = 40\%$ (red arrows) and at $h_s = 80\%$ (blue arrows).

Note that d_c can be obtained from the combination of Eq. (5) for ^{2}H and ^{18}O, which leads to the following expression, if we assume $R_\ell = R_{\mathrm{VSMOW2}}$:

$$d_c = \left\{ \frac{1}{\alpha^{2}_{\mathrm{H}}[\alpha_k^{2_{\mathrm{H}}} + h_s(1-\alpha_k^{2_{\mathrm{H}}})]} - 1 \right\} 1000 - 8 \left\{ \frac{1}{\alpha^{18}_{\mathrm{O}}[\alpha_k^{18_{\mathrm{O}}} + h_s(1-\alpha_k^{18_{\mathrm{O}}})]} - 1 \right\} 1000. \quad (6)$$

This very close to linear dependency of d_c on h_s is shown in Fig. 2a. The sensitivities of the slope and intercept of the $d_c(h_s)$ relation on the equilibrium fractionation factor α are weak (Fig. 2). In contrast, the variation of the nonequilibrium fractionation factor α_k as a function of wind speed $|U|^{10\,\mathrm{m}}$ when using α_k(MJ79) and the differences between the three α_k formulations are at least as important as the SST-induced shift in the intercept of the $d_c(h_s)$ relation (colored lines in Fig. 2). The impact of boundary layer turbulence and stability on α_k is not yet well constrained for the open sea and is based on ideal laboratory experiments performed in near-neutral stability conditions. According to Eriksson and Bolin (1964), 95% of present-day ocean evaporation occurs in the "smooth" regime. This is confirmed by the presently available observations of marine boundary layer d_v (Steen-Larsen et al. 2014, 2015; Benetti et al. 2014), which show that their identified $d_v(h_s)$ relations correspond better to α_k(MJ79) slopes in the smooth regime than the slopes in the rough regime. However, given that $|U|^{10\,\mathrm{m}}$ during SLOE is approximately $9\,\mathrm{m\,s^{-1}}$, the rough regime dominates the d_c calculated with α_k(MJ79).

Figure 1 illustrates the potential importance of the feedback of d_v (along the y axis) on d_e (colored shading), which is neglected when using the closure assumption (black line in Fig. 1). From a dynamical point of view, d_v can be different from d_e when strong, large-scale advection and/or vertical mixing prevails, in particular during the summer, when continental evaporation is large, downstream of land areas. The strength of the feedback effect of ambient d_v on d_e is humidity and wind-speed dependent (more important for high humidities and stronger winds), as illustrated in Fig. 1.

Far excursions from the closure assumption (deviations from the black line along the y axis in Figs. 1a,b) are rather unlikely, particularly in the case of strong evaporation, meaning for low h_s, in which case the new evaporate will rapidly change ambient d_v. For low ambient h_s, large differences between d_v and d_e are needed to significantly impact d_e. A deviation of ±5‰ for d_v from closure (see red arrow in Fig. 1a at $h_s = 40\%$) due to horizontal advection of an air mass with a distinct isotope signature at the evaporation site will lead to a small change in the resulting d_e (see red arrow on the color bar in Fig. 1a), when using CG65. Furthermore, very dry depleted continental or upper-tropospheric air is generally associated with high d_v, as discussed in several recent measurement studies (e.g., Kurita et al. 2016; Sodemann et al. 2017), because of the sensitivity of

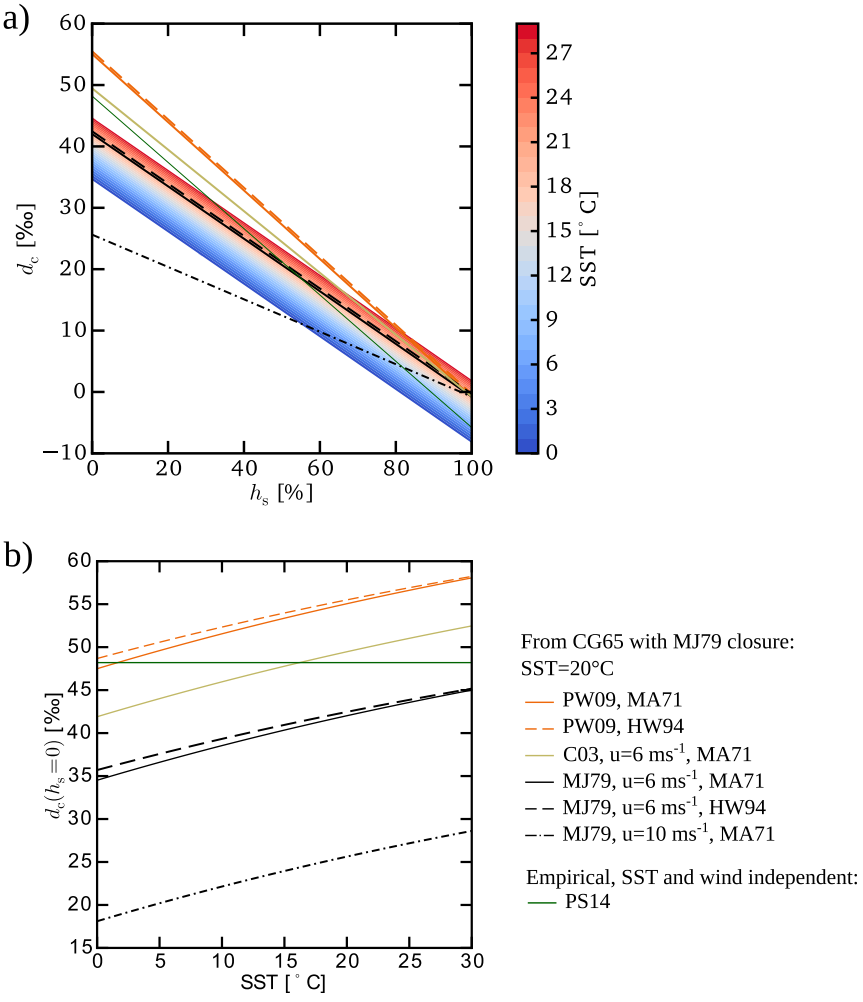

FIG. 2. (a) Closure deuterium excess in ocean evaporation d_c as a function of h_s with SST (colored shading) and $|U|^{10\,\mathrm{m}}$. (b) Intercept of the $d_c(h_s)$ relation as a function of SST and $|U|^{10\,\mathrm{m}}$. The lines show properties of the $d_c(h_s)$ relation assuming closure at SST = 20°C in (a) and for variable SST in (b) for different equilibrium fractionation factors α [Majoube 1971 (hereinafter MA71); Horita and Wesolowski 1994 (hereinafter HW94)] and nonequilibrium fractionation factors α_k [Cappa et al. 2003 (hereinafter C03); PW09; MJ79]. The empirical $|U|^{10\,\mathrm{m}}$ and SST-independent $d_c(h_s)$ relation from Pfahl and Sodemann (2014) are shown in green.

the traditional d definition on Rayleigh distillation at low humidity (Dütsch et al. 2017). Thus, the dry background airstream's d_v signature is generally not far from the d_v signature that it acquires during moistening by ocean evaporation.

In contrast to typical SLOE conditions with low h_s, d_e is very sensitive to d_v for high h_s, when evaporation is generally weaker. When comparing the blue and red arrows on the color bar in Fig. 1a the same deviation of ±5‰ of d_v from closure leads to a small impact on d_e for h_s = 40% and to a comparatively large impact for h_s = 80%. We thus expect d_e to be organized around the close neighborhood of the black line for $h_s < 60\%$ [during SLOE; see also section 3c in Part I)] and with a larger spread around the closure line for $h_s \geq 60\%$ (during no SLOE).

An isotope-enabled numerical model such as the isotope-enabled regional Consortium for Small-Scale Modeling Model ($\mathrm{COSMO_{iso}}$) includes the influence of the d_v feedback on d_e and thus provides an ideal test bed for investigating the validity of the closure hypothesis during SLOE. In a 3-month winter simulation with $\mathrm{COSMO_{iso}}$ (Pfahl et al. 2012) over the North Atlantic, we find relatively small deviations of d_e from d_v during SLOE of 2‰–6‰ and much larger deviations of more than 10‰ for no-SLOE conditions (see appendix A for further technical information on the $\mathrm{COSMO_{iso}}$ simulation and the adapted SLOE identification procedure). Note that

the differences between closure and nonclosure d_v found by Jouzel and Koster (1996), as well as in the above-mentioned $\text{COSMO}_{\text{iso}}$ simulation, are generally smaller than the uncertainty of 3‰–7‰ for the presently available measurements (e.g., Aemisegger et al. 2012; Bonne et al. 2014; Bailey et al. 2015; Steen-Larsen et al. 2015).

No direct validation of predicted SLOE d_c using the CG65closure is conducted in this study using measurements. For the years 2011–13 the obtained values for seasonal SLH-weighted mean d_c were compared to the few year-around water vapor measurements available from ocean-close setups (three stations in the North Atlantic and one station in eastern China). The results are shown (see Table B1) and discussed briefly in appendix B. We only mention here that the performance of the DJF d_c compares best with the observations when using α_k(MJ79cstu6ms) with a maximum seasonal deviation of 2.8‰ in the case of Ivittuut, Greenland. The seasonal means of d_c for α_k(PW09) mostly show a positive bias, whereas the seasonal means of d_c for α_k(MJ79) instead feature a low bias in estimated d_c.

To summarize, we discussed two major arguments related to why the closure assumption is likely to be fulfilled during SLOE conditions: 1) SLOE airstreams take up a large amount of humidity from ocean evaporation (Part I), thus overwriting the airstream's background d signature, and 2) when using the CG65 model [Eq. (3)] at low h_s, the background d_v influence is much weaker because of the smaller weighting in the CG65 equation than at high h_s, as illustrated in Fig. 1.

3. Results and discussion

a. *SLOE-induced d_c anomalies and the role of cyclones for d_c variability*

The 6-hourly d_c fields obtained using different α_k show similar spatial patterns but clear differences in absolute values (Figs. 3a–c). High d_c values are generally found inside SLOE features for all α_k. As expected from comparing the linear relationship in Fig. 2a, the highest d_c values are obtained when using α_k(PW09) (Fig. 3b) and lowest when using α_k(MJ79). From a comparison with seasonal measurement data (appendix B; see Table B1), we find that when using α_k(PW09) the d_c data suffer from an apparent high bias and when using α_k(MJ79) the d_c data suffer from an apparent low bias. In the case of α_k(PW09), this might come from the fact that the measurement data used to obtain this parameterization stem from the eastern Mediterranean Sea and were associated with a specific wind or boundary layer stability regime. In addition, the influence of nonresolved mixing with local land sources might have played a role as the measurement station used in PW09 is located 10 km from the Israeli coast in Rehovot. In the case of α_k(MJ79) the low d_c values come from the wind dependency of the α_k formulation, which has a strong impact, not only on the 6-hourly d_c patterns, but also at monthly and annual time scales and the $d_c(h_s)$ and d_c(SST) relations, as discussed in sections 3b and 3d below. Additionally to the lower d_c values in Fig. 3a for α_k(MJ79) compared to the wind-independent α_k formulations in Figs. 3b,c, the d_c field in Fig. 3a shows abrupt changes of d_c values that are due to the step change in the wind regime at 7 m s^{-1}. The wind dependency of α_k(MJ79) induces maxima of d_c that are slightly displaced compared to the two other α_k parameterizations, sometimes these maxima are found at the border or even outside the SLOE features.

The same tendency has already been mentioned for the 6-hourly fields is true for the cold season mean fields for the different α_k (Fig. 4) and the mean conditions for all SLOE objects in the North Atlantic (Table 1). Highest wintertime d_c values are found for α_k(PW09) (Figs. 4c,d), lowest values for α_k(MJ79) (Figs. 4a,b), and intermediate values for α_k(MJ79cstu6ms) (Figs. 4e,f). Wintertime composites of d_c during SLOE reveal higher d_c than the SLH-weighted seasonal means for all α_k in the extratropics (cf. Figs. 4b,d,f and Figs. 4a,c,e). For α_k(MJ79) only, very small differences in the seasonal means are found in the subtropics (Figs. 4a,b). For α_k(PW09) and α_k(MJ79cstu6ms), the d_c differences between the SLOE composites and the SLH-weighted means are in the range of 2‰–8‰, and higher values in the SLOE composites than in the SLH-weighted means. This highlights again the strongly anomalous conditions in h_s and near-surface wind speeds during SLOE compared to average evaporative conditions, as discussed in Part I. The patterns of the d_c fields are otherwise similar between the SLOE composites and the SLH-weighted means for a given α_k. Highest SLOE d_c values are found along the warm WBCs and along the sea ice edge and in the northern latitudes of the North Atlantic. Both regions are associated with $h_s < 60\%$ during SLOE. When including the effect of SST, the high-latitude cold season d_c values are substantially lower than those obtained by the measurement-based linear regression prediction based solely on h_s from Pfahl and Sodemann (2014). The lowest SLOE d_c values are found in regions associated with $h_s > 60\%$ and strong near-surface winds. The same spatial d_c distribution is reflected in the wintertime cyclone composites shown in Fig. 5a, albeit with approximately 5‰–10‰ lower d_c values than in the SLOE composites. A large part of the cyclone area is generally associated with warm-air advection, high h_s, and thus lower d_c. The contrasts between the d_c values in the SLOE composites and the cyclone composites highlight the importance of these features in the modulation of the d_c signature.

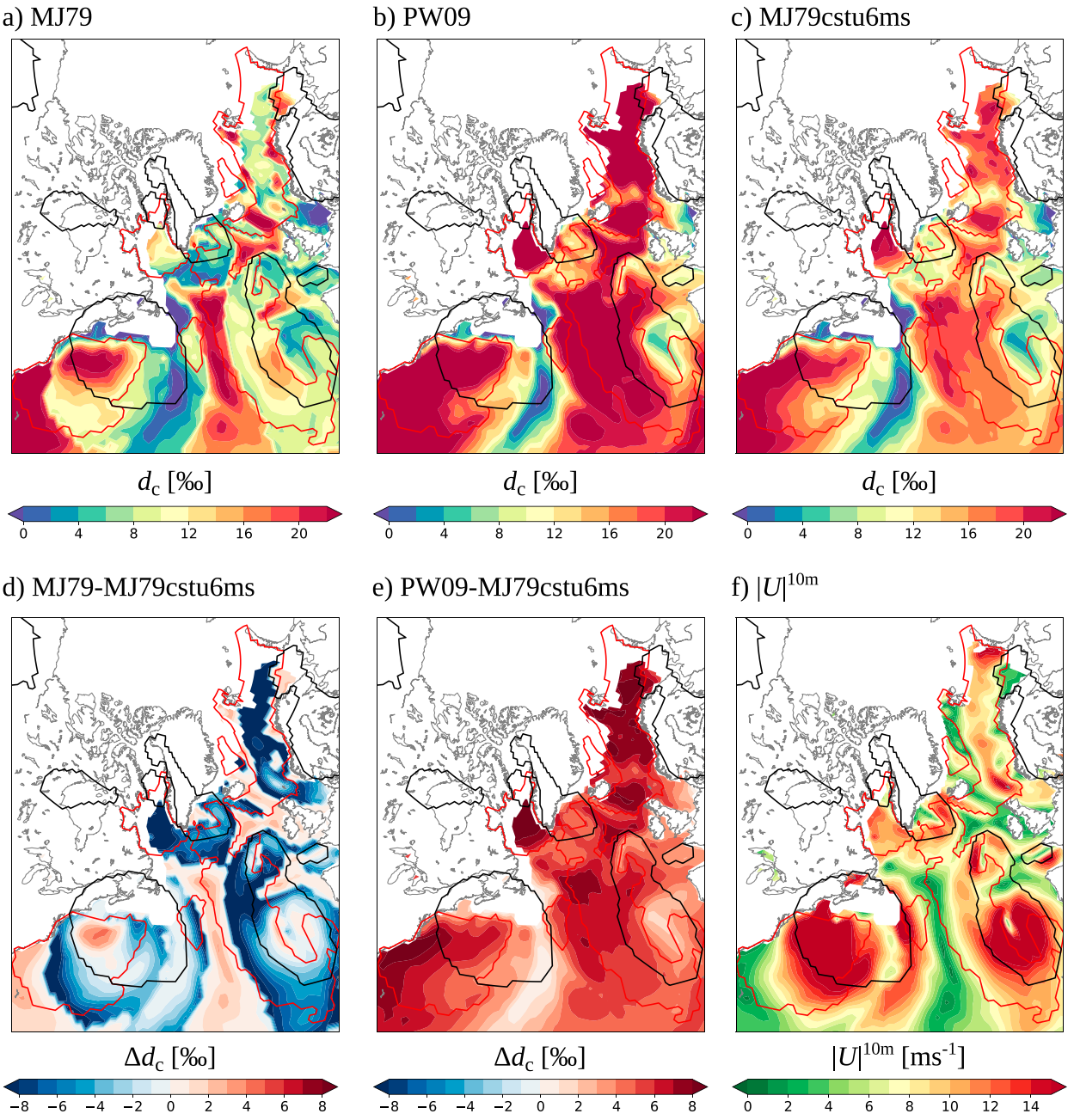

FIG. 3. Closure deuterium excess in ocean evaporation d_c (colored shading) for different nonequilibrium fractionation factors α_k at 1800 UTC 1 Mar 2010 in the North Atlantic: (a) α_k from MJ79, (b) α_k from PW09, and (c) α_k from MJ79 without wind-speed dependency and α_k(MJ79) taken at $|U|^{10\,\mathrm{m}} = 6\,\mathrm{m\,s^{-1}}$ (MJ79cstu6ms). Differences (d) between d_c with α_k(MJ79) and d_c with α_k(MJ79cstu6ms) and (e) between d_c with α_k(PW09) and d_c with α_k(MJ79cstu6ms) are shown. (f) Since d_c with α_k(MJ79) is strongly affected by $|U|^{10\,\mathrm{m}}$, this field is shown for reference. SLOE features using the evaporation efficiency parameter $f_{\mathrm{pw}} \geq 1.5\,\mathrm{h^{-1}}$ in Part I are shown with red contours, and the cyclone regions are shown with black contours. Land areas, regions covered with sea ice, or where SLH $\geq 0\,\mathrm{W\,m^{-2}}$ (SLH from the atmosphere to the ocean) are masked in white and correspond to areas with $h_s > 90\%$.

b. Direct and indirect effects of h_s and SST on d_c

When applying the CG65closure formulation for determining d_c, h_s, and SST are the main environmental controlling variables. Additionally $|U|^{10\,\mathrm{m}}$ is important if α_k(MJ79) is used. We will first focus on h_s and SST and their influence on d_c for α_k(MJ79cstu6ms) and then discuss the influence of $|U|^{10\,\mathrm{m}}$ on the d_c–h_s and d_c–SST correlations when using α_k(MJ79). We use the SLOE framework and the closure assumption to discuss the

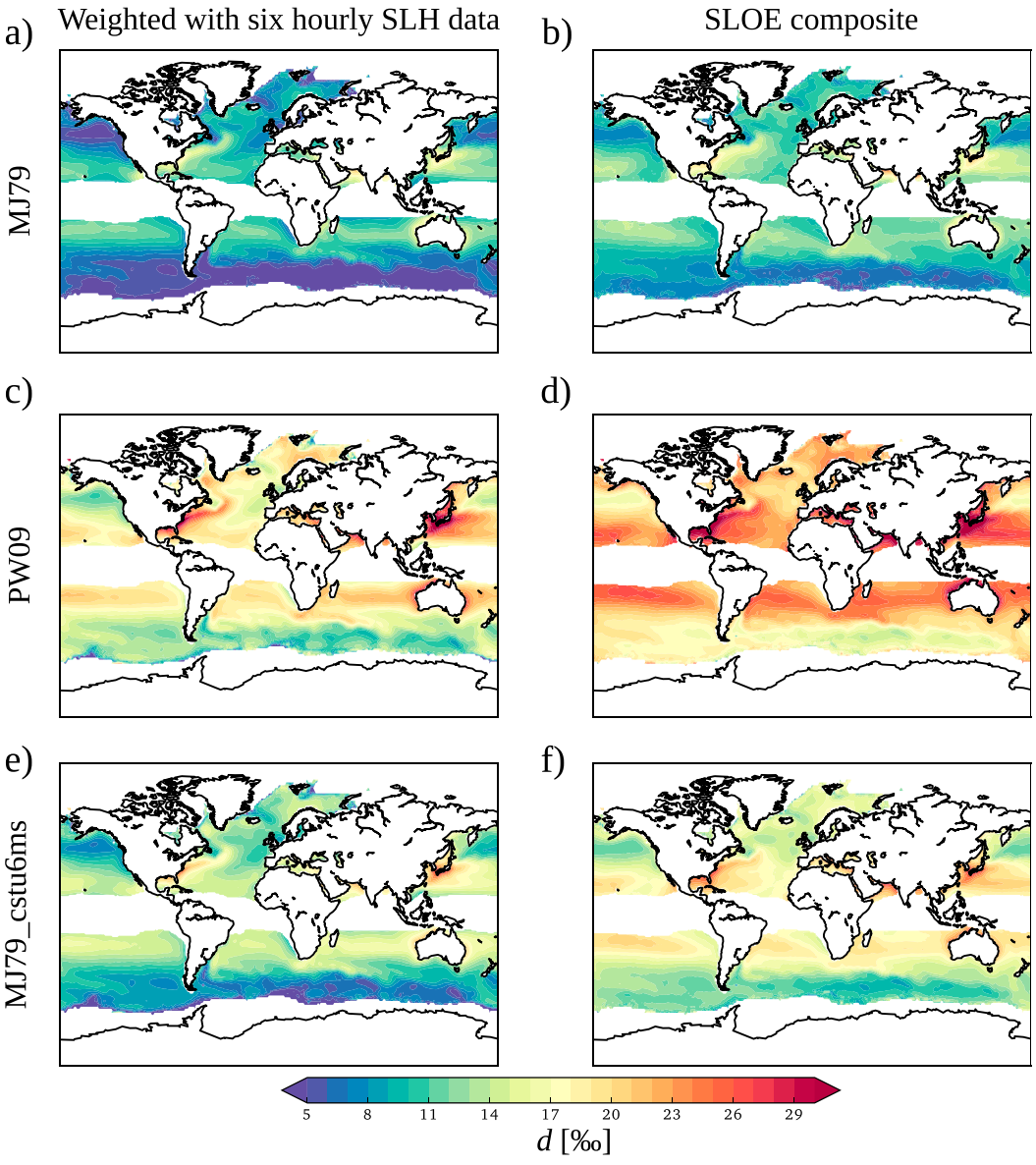

FIG. 4. (a),(c),(e) Winter (DJF for the Northern Hemisphere and JJA for the Southern Hemisphere) SLH-weighted means and (b),(d),(f) SLOE composites of d_c for the period 1979–2014, for (a),(b) α_k(MJ79), (c),(d) α_k(PW09), and (e),(f) α_k(MJ79cstu6ms). Land areas, regions with seasonal mean SLOE frequencies below 1% (tropics), or areas with seasonal sea ice (seasonal mean SST $\leq$ 0°C) are masked.

relationship between d_c and its controlling variables. Within a nonclosure framework the described relationships are impacted by the past history of the water vapor present at the site of evaporation and we expect the d_c–h_s and d_c–SST correlations to be weakened particularly in conditions of high h_s. Figure 6 illustrates the direct and indirect controls of h_s and SST on d_c. The direct controls are those coming from the variable itself as it enters into the CG65closure parameterization. The direct controls shown by thick arrows in Fig. 6 represent a positive relationship between SST and d_c that comes from the SST dependency of α and a negative relationship between h_s and d_c that reflects the stronger non-equilibrium fractionation effects for larger near-surface humidity gradients (as also illustrated in Fig. 2). Indeed, the highest d_c values are found in regions of warm SSTs during cold-air advection, inducing strong humidity gradients toward the sea surface as, for example, along the warm WBCs (Fig. 4). The indirect controls are those emerging from cross correlations between h_s and SST

TABLE 1. Values for d_c during SLOE in the North Atlantic (30°–90°N, 100°W–100°E) during the period 2010–14.

	Mean	Std dev	10th percentile	90th percentile
d_c for MJ79 (‰)	12.3	5.3	7.2	18.7
d_c for PW09 (‰)	23.0	5.6	15.8	30.4
d_c for MJ79cstu6ms (‰)	16.9	4.6	10.9	23.0

(black arrows in Fig. 6). Two regimes can be found, when looking more closely at the nature of the h_s–SST relationship:

1) A positive feedback regime reinforces the CG65closure direct controls, in which a *negative* correlation between h_s and SST is found. At the interannual time scale this regime is strongest along the warm WBCs, associated with "warm ocean" SLOE and characterized by rapid moisture export (Fig. 7b; see also the discussion on SLOE types in Part I). At monthly to seasonal time scales, although weak, it is generally found equatorward of 50°N and 50°S with its strongest impact at the eastern subtropical boundaries of the large ocean basins (Fig. 7a). In this regime, the SST variability dominates the strength of air–sea interactions. The regression slope of near-surface air temperature (SAT) with respect to SST is <1 (Figs. 7g,h). The changes in the specific humidity of the air q_a are smaller than the SST induced changes in the saturation specific humidity with respect to SST q_s. Higher SSTs thus induce stronger air–sea humidity gradients (i.e., lower h_s). In this positive feedback regime, the d_c–SST correlations are positive (Figs. 7c,d), which corresponds to the traditionally assumed dominating regime over long time scales for the interpretation of d in ice cores (e.g., Johnsen et al. 1989; Vimeux et al. 1999; Stenni et al. 2001).
2) A negative feedback regime weakens the CG65closure direct controls, in which a *positive* correlation between h_s and SST is found. This regime is particularly pronounced at high latitudes and at monthly–seasonal time scales (Fig. 7a). Higher SSTs in summer go along with weaker air–sea humidity gradients (i.e., higher h_s), and conversely lower SSTs in winter appear when the effects of cold-air advection are strongest and the humidity depletion of the air is largest. This is the seasonal cycle that is reflected in extratropical precipitation d_p from the Global Network of Isotopes in Precipitation (GNIP; IAEA/WMO 2018; Araguás-Araguás et al. 2000) as described by Pfahl and Sodemann (2014). At the interannual time scale this regime is predominant in regions of high $|U|^{10\,\mathrm{m}}$ along the storm track northeast of Newfoundland and Japan in the Northern Hemisphere and along the winter sea ice edge in the Southern Hemisphere (Fig. 7b). In this regime, the direct controls on d_c are weakened. This has a strong impact on the d_c–SST relationship, which is even reversed compared to the positive d_c–SST relationship resulting from the direct CG65closure control (Figs. 7c,d). The SAT variability dominates the air–sea temperature and humidity gradient, and the regression slope of SAT with respect to SST is >1 (Figs. 7g,h). The changes in q_a are larger than the SST-induced changes in q_s. The thermodynamical properties of the air masses (SAT and q_a) shape the variability of h_s. The preconditioning of these air masses and their large-scale flow is the determining

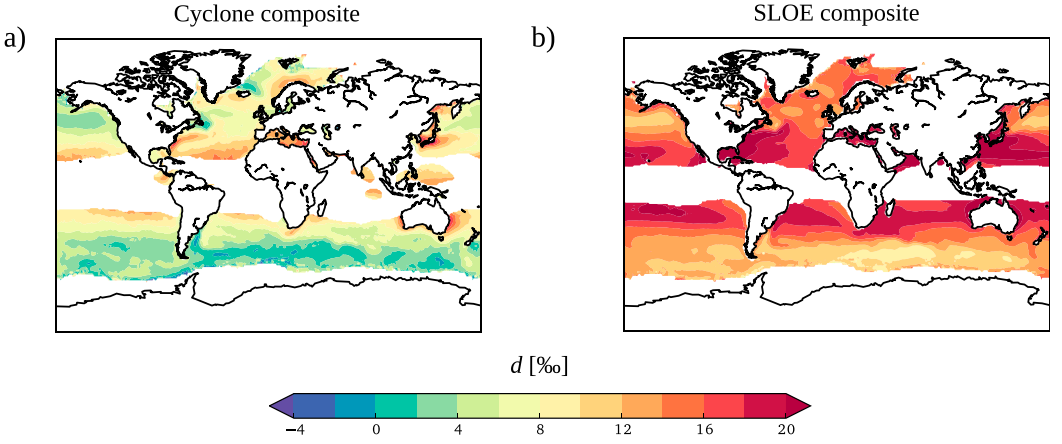

FIG. 5. Winter composites (DJF for the Northern Hemisphere and JJA for the Southern Hemisphere) of d_c for the period 1979–2014 during (a) cyclone passages and (b) SLOE for α_k(MJ79cstu6ms). Land areas, regions with seasonal sea ice, or with occurrence frequencies smaller than 1% for cyclones in (a) or SLOE in (b) are masked.

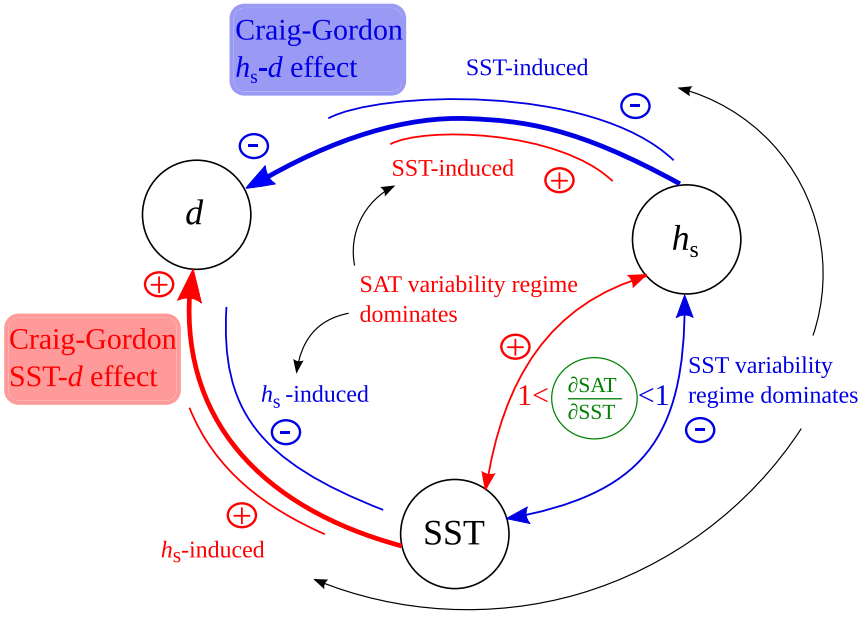

FIG. 6. Schematic of the main direct and indirect controlling mechanisms of h_s and SST on d_c. The direct controlling mechanisms are those exerted by h_s and SST through the CG65closure model, namely a positive relationship between SST and d_c (through α) and a negative relationship between h_s and d_c. These direct controls can be reinforced, attenuated, or even inverted depending on the sign and strength of the cross-correlation effects between h_s and SST. The sensitivity of SAT to SST (∂SAT/∂SST) controls the sign and amplitude of the cross correlation between h_s and SST. If the variability in q_s is larger than q_a, the variability of $h_s = q_a/q_s$ will be primarily controlled by the SST. Higher q_s thus induces lower h_s. If q_a varies more than q_s, h_s will be primarily determined by SAT. Higher q_a thus induces higher h_s. In summary, for ∂SAT/∂SST < 1, the SST variability regime dominates; in this case the SST and h_s are negatively related. The negative h_s–SST cross correlation reinforces the CG65closure controls on d_c. If, on the contrary, ∂SAT/∂SST > 1, the SAT variability regime dominates and the SST and h_s are negatively related. The positive h_s–SST cross correlation weakens the CG65closure controls on d_c. Wind speed and boundary layer stability, which are not represented here, may influence α_k and through it the $d_c(h_s)$ and d_c(SST) relations.

factor for the h_s–SST relationship. The regions associated with this regime at the monthly time scale and partly also at the interannual time scale are regions of net moisture convergence mainly coinciding with "wind driven" and "polar air" SLOE.

Note that the correlation patterns found here for SLOE are similar to the patterns found when using SLH-weighted monthly and annual means and the same interpretations are valid (not shown). The cross correlation between h_s and SST is particularly important for the d_c–SST relationship as it can invert the sign of this relationship in certain regions (Figs. 7c,d). The d_c–h_s relationship is only weakly or not impacted by h_s–SST cross-correlation effects (Figs. 7e,f). The strength of the d_c–h_s relationship is only notably affected at the monthly time scale (Fig. 7e) in regions with a strong d_c–SST relationship and a weak h_s–SST relationship [$r(h_s, \text{SST}) \sim 0$]. These are interesting regions to study more closely using measurements, for example, from Bermuda (Steen-Larsen et al. 2014) or Japan to gain further process understanding. In these regions, SST might play a more important role in d_c variability than at other locations. The strong negative relationship between d_c and h_s is also clearly reflected in recent synoptic time-scale measurements in the Mediterranean Sea (Angert et al. 2008; Pfahl and Wernli 2008), the North Atlantic (Steen-Larsen et al. 2013, 2014; Benetti et al. 2014), as well as the Southern Ocean (Uemura et al. 2008). A clear positive correlation between d_c and SST (positive feedback regime) is only found for the part of the expedition from Antarctica to Australia in Uemura et al. (2008) . It must be stressed that the correlation found by Uemura et al. (2008) was a spatial correlation. Indeed, as shown by Brown and Simmonds (2004), the isotope–climate relationships are not invariant and depend on the specific distribution of continents and atmospheric flow regimes. Pfahl and Wernli (2008) found a weak negative

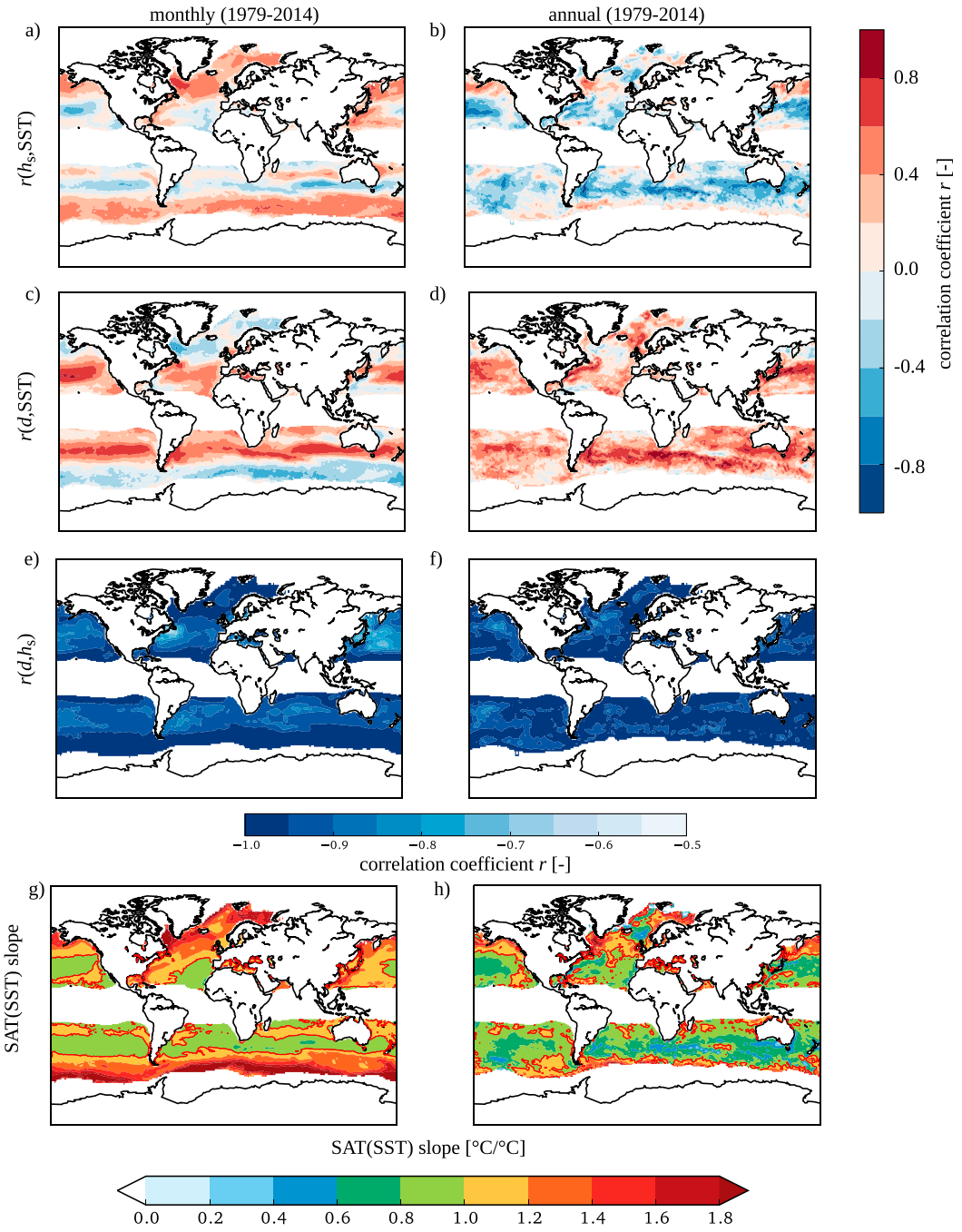

FIG. 7. Correlation of h_s and SST using (a) monthly composite data and (b) annual composites during SLOE. Correlation between d_c estimated with α_k(MJ79cstu6ms) and SST using (c) monthly composite data and (d) annual composites. Correlation between d_c estimated with α_k(MJ79cstu6ms) and h_s using (e) monthly composite data and (f) annual composites. The SAT (SST) linear regression slopes for (g) monthly and (h) annual composites. The red contours in (g) and (h) highlight the SAT (SST) slope of 1°C °C^{-1}. The correlation and SAT (SST) slope maps are composites obtained from the conditions during SLOE events during the period 1979–2014. For α_k(PW09), the correlation patterns between d_c with h_s and d_c with SST look similar. [For α_k(MJ79), the correlation fields are weaker and are shown for monthly data in Fig. 8.] All the patterns look similar when using SLH-weighted monthly composites instead of composites during SLOE conditions. Land areas, regions with seasonal mean SLOE frequencies below 1% (tropics), or areas with seasonal sea ice are masked.

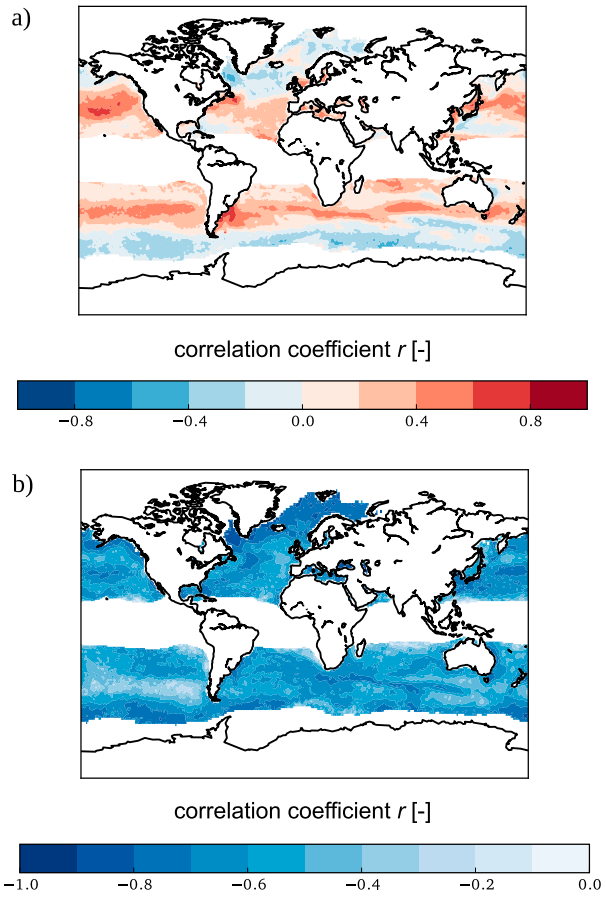

FIG. 8. Correlation of (a) d_c with SST and (b) d_c with h_s using monthly mean data and α_k(MJ79) during SLOE. Both patterns look similar when using SLH-weighted monthly means. Land areas, regions with seasonal mean SLOE frequencies below 1% (tropics), or areas with seasonal sea ice are masked.

temporal d_c–SST correlation for the Mediterranean Sea (negative feedback regime).

When including the effect of $|U|^{10\,\mathrm{m}}$ on α_k by using α_k(MJ79), the correlation patterns of SST and h_s with d_c are substantially weakened, as shown in Fig. 8 using monthly mean composites of SLOE conditions, especially for regions of high $|U|^{10\,\mathrm{m}}$, where d_c–h_s correlations of <0.4 are found. The important consequences of these weakened correlations of d_c with its primary control variables on the resulting linear sensitivity estimates using α_k(MJ79) will be discussed in section 3d.

c. *Correlations between $|U|^{10\,\mathrm{m}}$ and d_c*

Correlations between d_c and $|U|^{10\,\mathrm{m}}$ for all the α_k are approximately -0.5 during SLOE. For the SLH-weighted d_c estimates a weak positive correlation is found of up to 0.5. Similar values but of opposite sign are obtained for the correlation between h_s and $|U|^{10\,\mathrm{m}}$. The expected positive influence of the wind speed on the evaporation strength probably leads to a weak positive correlation between d_c and $|U|^{10\,\mathrm{m}}$ in the SLH-weighted data. In the case of SLOE composites, the focus on strongly evaporative conditions appears to reverse the relationship between d_c and $|U|^{10\,\mathrm{m}}$. SLOE events with high wind speeds are generally associated with higher h_s and thus lower d_c than SLOE events with low winds, leading to the observed negative temporal d_c–$|U|^{10\,\mathrm{m}}$ relationship. The same tendency is visible in the spatial correlations of d_c and $|U|^{10\,\mathrm{m}}$ during SLOE. Composites of SLOE show maxima of $|U|^{10\,\mathrm{m}}$ (strongly "wind-driven SLOE") collocated with maxima of h_s (Part I) (i.e., minima of d_e). A prominent meridional band of maxima in $|U|^{10\,\mathrm{m}}$ during strong ocean evaporation at about 50°S and around 50°–60°N in the region of frequent cyclone passages has a corresponding band of maxima in h_s and minima in d_c (Fig. 4). The typical large-scale circulation associated with SLOE is thus probably responsible for the observed negative d_c–$|U|^{10\,\mathrm{m}}$ correlation.

d. *Sensitivity of d_c with respect to h_s and SST at the moisture source*

Because of the two existing regimes of cross correlation between h_s and SST described in section 3b, the sensitivities of d_c compared to h_s and SST are not spatially uniform as shown for monthly and annual data in Figs. 9 and 10. Note that only univariate linear regression slope estimates are discussed here. Multivariate sensitivity estimates lead to slightly different values and are of secondary importance, if the final aim is to invert the relationship and use d from natural archives as a climate proxy. We start by first discussing the spatial variability the $d_c(h_s)$ slope and then the d_c(SST) slope during SLOE. At the end of this section we present a more detailed analysis of these $d_c(h_s)$ and d_c(SST) sensitivities for the North Atlantic using average conditions in individual SLOE features occurring during the period 2010–14 (30°–90°N, 100°W–100°E; Table 2 and Fig. 11).

For α_k(MJ79cstu6ms) a global-mean $d_c(h_s)$ slope of $-0.42‰ \pm 0.05‰\,\%^{-1}$ when using monthly composites is found with a small spatial variability (Fig. 9b). This value is close to the slopes found in studies based on near-surface water vapor measurements, in which linear $d_c(h_s)$ relations with slopes from $-0.42‰\,\%^{-1}$ to $-0.58‰\,\%^{-1}$ were found to fit the observations relatively well in the North Atlantic (Benetti et al. 2014; Bonne et al. 2014; Steen-Larsen et al. 2015) as well as in the Southern Ocean (Uemura et al. 2008). For α_k(PW09), a $d_c(h_s)$ slope of $-0.52‰ \pm 0.03‰\,\%^{-1}$ is found [not shown; same patterns as for α_k(MJ79cstu6ms)]. This slope is close to the one found in a study based on measurements in the eastern Mediterranean Sea (Pfahl and Wernli 2008).

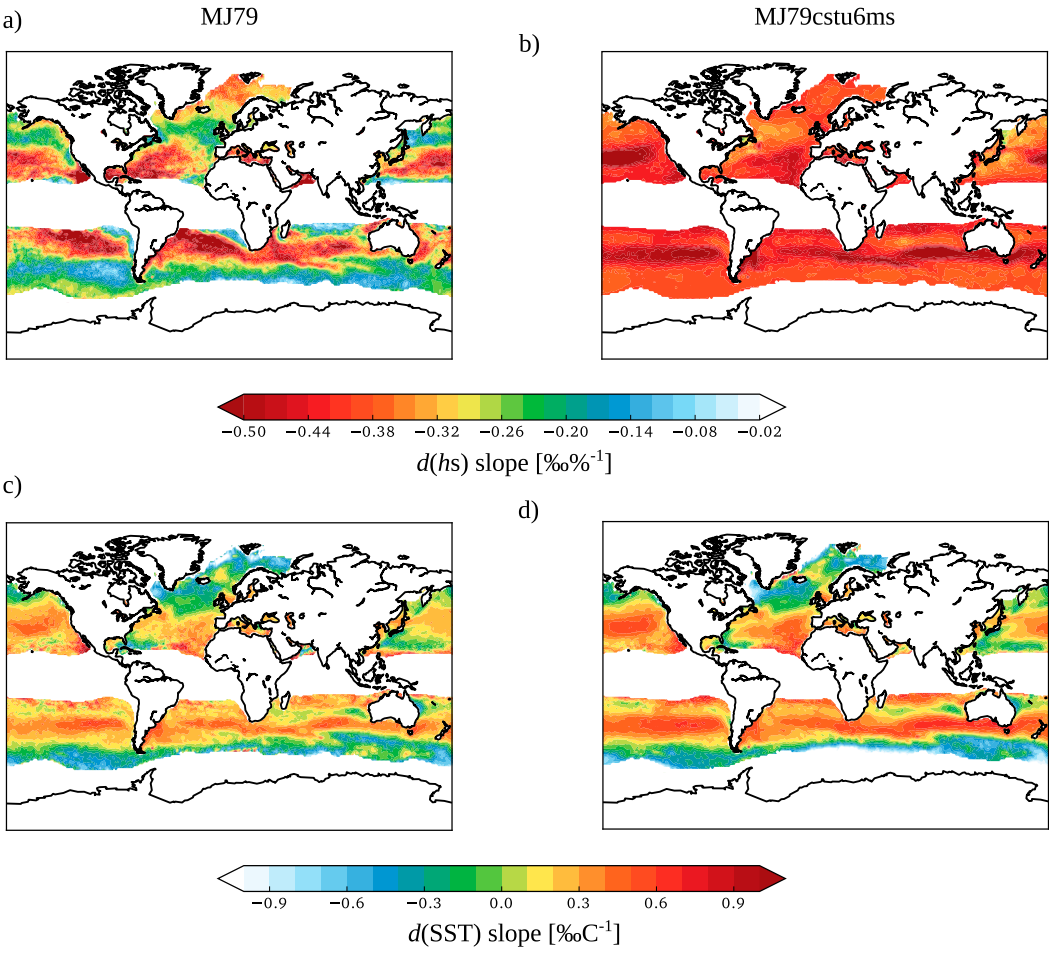

FIG. 9. Regression slopes (univariate) of monthly mean composites during SLOE of (a),(b) $d_c(h_s)$, (c),(d) d_c(SST), using (a),(c) α_k(MJ79) and (b),(d) α_k(MJ79cstu6ms). Land areas, regions with seasonal mean SLOE frequencies below 1% (tropics), or areas with seasonal sea ice are masked.

The $d_c(h_s)$ slopes tend to become slightly steeper with longer averaging time scales for the wind-independent α_k (cf. Figs. 9b and 10b). A steepening tendency of the $d_c(h_s)$ slope for data averaged from 1 day to 2 weeks has also been mentioned by Steen-Larsen et al. (2014) for measurements in Bermuda.

For α_k(MJ79) the effect of $|U|^{10\,\mathrm{m}}$ on the $d_c(h_s)$ slope estimate is considerable. The $d_c(h_s)$ slope shows strong spatial variability (Figs. 9a and 10a). The steepest slopes with comparable values to the estimates from the wind-independent α_k formulations are found in regions where the smooth wind regime is more frequent than the rough regime, especially at lower latitudes, in the subtropics, and along the warm WBCs. Much flatter $d_c(h_s)$ slopes with values between $-0.1‰$ and $-0.3‰\ \%^{-1}$ are found elsewhere. Such flat $d_c(h_s)$ slopes have only been documented over land (Welp et al. 2012; Aemisegger et al. 2014); however, they have not yet been found in measurements from the marine boundary layer. The $d_c(h_s)$ slopes using α_k(MJ79) can become particularly flat in areas of high $|U|^{10\,\mathrm{m}}$ along the storm tracks.

As opposed to the $d_c(h_s)$ relation, a strong spatial variability in the d_c(SST) slopes covering the whole range between $-1‰$ and $+1‰\ °C^{-1}$ is found for all α_k (Figs. 9c,d and 10c,d). Furthermore, the same steepening tendency as for the $d_c(h_s)$ relation for increasing averaging time scales is observed for the global-mean d_c(SST) slope, which increases from $0.14‰ \pm 0.36‰$ to $0.52‰ \pm 0.37‰\ °C^{-1}$ for α_k (MJ79cstu6ms). Our analysis from section 3b above suggests that this tendency is related to changes in the h_s–SST feedback regime on d_v for longer time scales. When using annual mean composites, the negative h_s–SST relationship becomes stronger, particularly over the warm WBCs and tends to reinforce the direct CG65closure control on the d_c(SST) relation, leading to the observed steepening of the d_c(SST) slope.

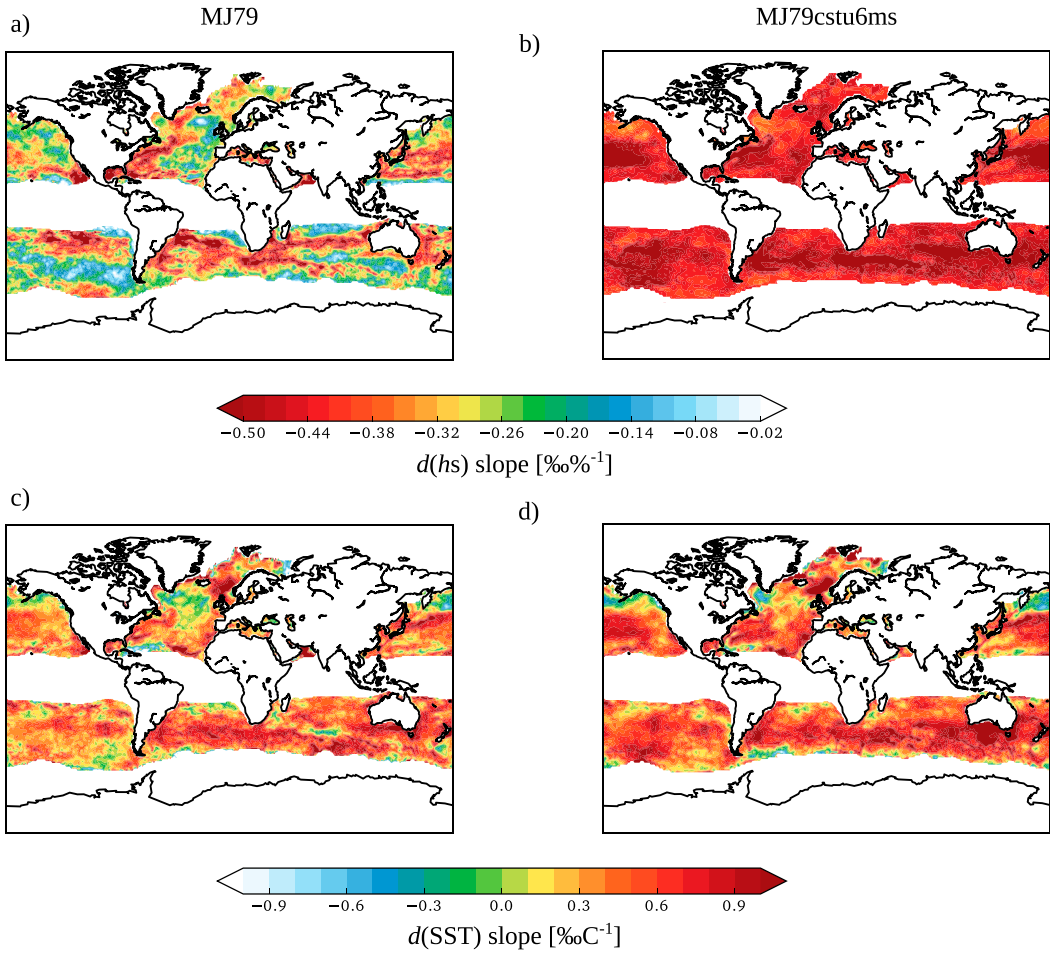

FIG. 10. As in Fig. 9, but using annual composites during SLOE.

The spatial d_c(SST) sensitivity patterns from the α_k(MJ79) formulation are similar to the ones from the wind-independent α_k, although with attenuated amplitude (Figs. 9c,d and 10c,d).

To investigate the $d_c(h_s)$ and d_c(SST) slopes at the oceanwide scale and focusing on average conditions associated with individual SLOE events, a more detailed SLOE object-based analysis was performed for the North Atlantic between 2010 and 2015. In Fig. 11, the same differences in $d_c(h_s)$ slopes for different α_k formulations as described above for the gridpoint-based analysis for the full ERA-Interim period can be observed. The large uncertainty bars shown in gray in Fig. 11 reflect the sometimes large variability in h_s and d_c conditions across a single SLOE object. The distribution of h_s beneath the x axis in Fig. 11c highlights the high frequency of SLOE events that are associated with low h_s conditions. The 10th–90th percentile range for h_s encompasses values between 40% and 65%. The slopes and correlations of the $d_c(h_s)$ and the d_c(SST) relations for the SLOE-based North Atlantic analysis are summarized in Table 2. The lowest d_c–h_s correlation is found for α_k(MJ79) and the highest for α_k(PW09). The MJ79 $d_c(h_s)$ slope of $-0.31‰\,\%^{-1}$ for the North Atlantic is much lower than the ones discussed above from published measurement datasets. The fact that simulations performed with isoGCMs in recent years have been nearly exclusively done using α_k(MJ79) might explain

TABLE 2. The $d_c(h_s)$ and d_c(SST) temporal regression slopes (univariate p values are all <0.01) and correlations from mean conditions during SLOE in the North Atlantic (30°–90°N, 100°W–100°E) in the 6-hourly fields of the period 2010–14 for the different α_k (see also scatterplots in Fig. 11). The standard error of the slope estimates are smaller than the indicated precision.

	MJ79	PW09	MJ79cstu6ms
$r(d_c, h_s)$	−0.67	−0.87	−0.81
$d_c(h_s)$ slope ($‰\,\%^{-1}$)	−0.31	−0.52	−0.42
$r(d_c$, SST)	0.52	0.48	0.58
d_c(SST) slope ($‰\,°C^{-1}$)	0.28	0.25	0.34

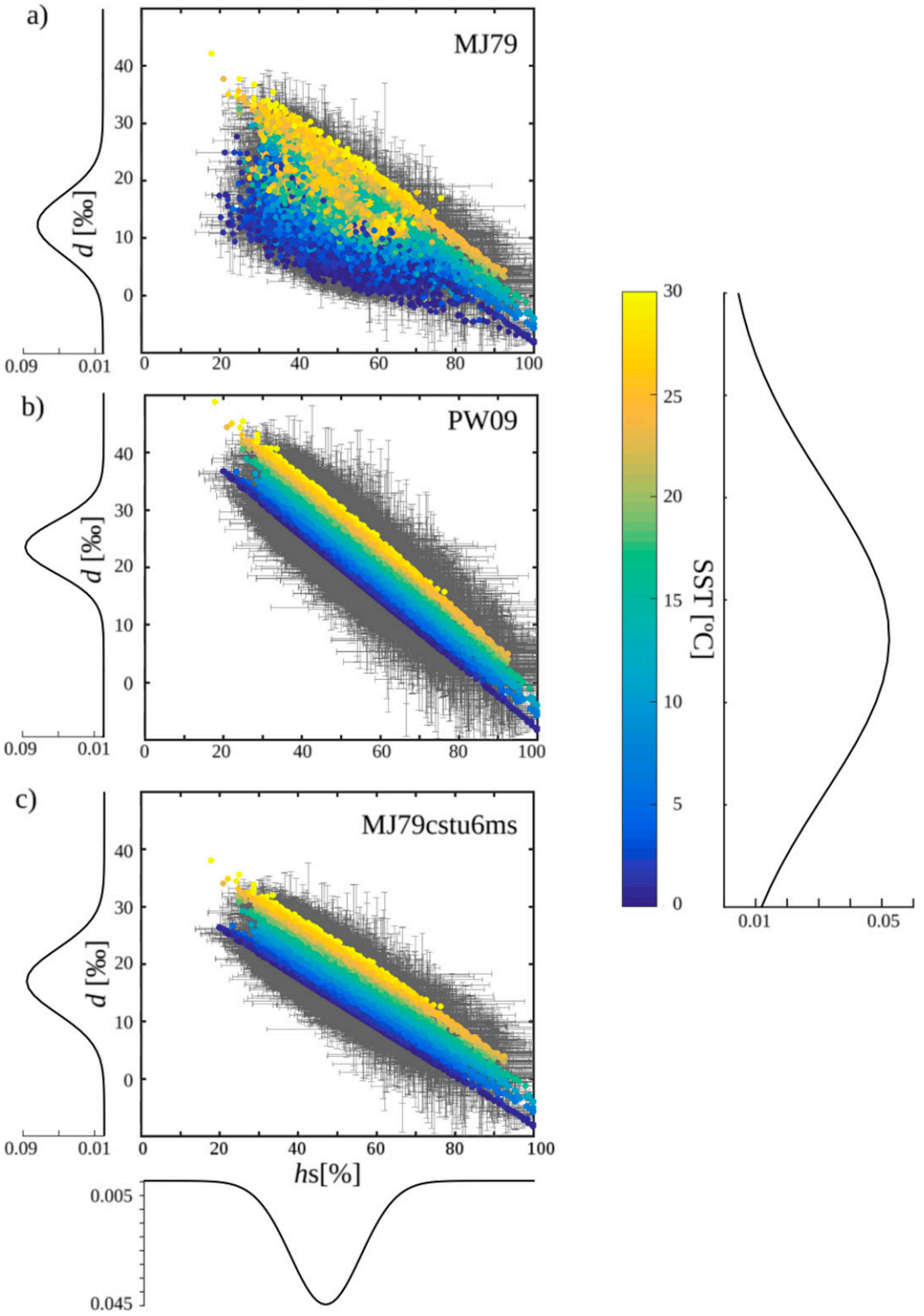

FIG. 11. Scatterplots of mean conditions of SLOE objects for different α_k values in the North Atlantic (30°–90°N, 100°W–100°E). The standard deviation of the conditions for each SLOE object is shown with gray errorbars. Each point represents one SLOE object in the 6-hourly reanalysis fields during the period 2010–14.

part of the deficiencies of these models in representing the moisture source d_c. Indeed, better agreement with GNIP precipitation isotope measurement data using α_k(PW09) than α_k(MJ79) has been found by Dütsch (2016) in 10-yr climate simulations with $\text{COSMO}_{\text{iso}}$ (Pfahl et al. 2012).

Note that slightly steeper $d_c(h_s)$ slopes are found here for high SSTs than for low SSTs [$-0.38‰\,\%^{-1}$ for SST < 21°C and $-0.44‰\,\%^{-1}$ for SST > 26°C for α_k(MJ79cstu6ms)]. Steen-Larsen et al. (2014) also found steeper $d_c(h_s)$ slopes for SST > 26°C than for SST < 21°C in their near-surface atmospheric water vapor isotope measurements in the North Atlantic (see their Fig. 11c). This tendency of finding steeper $d_c(h_s)$ slopes in regions of warm ocean waters can also be observed in Figs. 9b and 10b and can be attributed to the positive feedback of SST through its cross correlation with h_s.

A particularly interesting subregion in the North Atlantic in terms of $d_c(h_s)$ and d_c(SST) slopes is the region of the Labrador and Irminger Seas, as well as the North Atlantic south of Iceland and east of Newfoundland (LISEI region in Part I). In the LISEI region, both slopes reach their North Atlantic minimum. The $d_c(h_s)$ slope is approximately $-0.35‰\,\%^{-1}$ and the d_c(SST) slope is negative, in the range from $-1‰$ to $0‰\,°\text{C}^{-1}$. Accordingly, this region stands out in the correlation analysis presented above in section 3b as affected by a strong positive cross correlation between h_s and SST at both monthly and interannual time scales. It is probable that the cyclone frequency in the Irminger Sea exerts a key control on this pattern of cross correlations. The cyclone frequency in the Irminger Sea is strongly linked with the North Atlantic Oscillation (NAO). One possible mechanism inducing a positive h_s–SST relationship is that more frequent cyclones during positive-phase NAO (NAO+) years induce more frequent cold-air outbreaks in the LISEI region. These cold-air outbreaks are in turn responsible for more frequent SLOE events that lower h_s and probably lead to evaporative cooling of the sea surface (Part I). This control of Irminger Sea storms on evaporation patterns in the LISEI region may be responsible for the positive cross correlation found here between h_s and SST in this region.

The marked change in SLOE frequency in the North Atlantic for NAO+ compared to negative-phase NAO (NAO−) years may be relevant for the source signature recorded in the stable water isotopic composition of moisture transported to Greenland. Indeed, distinctly higher d_p values in precipitation during NAO+ compared to NAO− have been found in western Greenland, where precipitation mainly originates from the LISEI region (Sodemann et al. 2008b). An opposite tendency with higher d_p for NAO− has been found for eastern Greenland, where the evaporative sources of precipitation are located in the eastern North Atlantic along the European coast with slightly lower h_s during NAO− compared to NAO+ (Fig. 10c in Part I). The isotope signature of Greenland precipitation thus seems to qualitatively reflect the dipole of NAO-induced changes in cold-air advection and SLOE over the midlatitude North Atlantic. To ascertain this link between Greenland d_p and SLOE frequency in the different regions of the North Atlantic, more detailed research will be necessary using measurement data from the marine moisture source and precipitation in Greenland. Additional factors such as cloud microphysical processes as well as the d definition problem (Dütsch 2016; Markle et al. 2017) can potentially alter the above-described moisture source isotope–climate relationship.

e. *Synthesis of the use of different nonequilibrium fractionation factors α_k*

We showed above that when using steep $d_c(h_s)$ slopes in the CG65closure framework such as with α_k(PW09) on a seasonal mean basis, very high d_c values are obtained, which show a positive bias with the few available year-round measurements particularly in autumn and winter. Flatter slopes such as those obtained with α_k(MJ79) however show negative biases with observations particularly in spring and summer (appendix B). The results with α_k(MJ79cstu6ms) presented here seem to correspond relatively well with what has been observed in recent measurements. However, a more thorough assessment also at high temporal resolution using measurements from the marine boundary layer would be needed to confirm this finding. It may be that from empirical field data a boundary layer stability and turbulence dependent formulation of α_k emerges, as has been suggested in previous literature (Craig and Gordon 1965; MJ79; Tanny and Cohen 2008), to take into account the different turbulent boundary layer regimes observed in different synoptic environments. The existing α_k(MJ79) parameterization that includes a wind-dependent parameterization reflecting changes in the laminar evaporation-layer properties and surface roughness leads to low-biased d_c estimates. This is mainly due to an overrepresentation of rough evaporation conditions, as shown here and in previous studies (e.g., Risi et al. 2013). This calls for an adapted wind- or stability-dependent formulation of α_k.

Following the general definition of α_k introduced by Craig and Gordon (1965) in analogy with the Pasquill–Sutton turbulence model (Pasquill 1943; Sutton 1934),

$$\alpha_k = \left(\frac{D}{D'}\right)^m, \tag{7}$$

where $\alpha_k > 1$, with a diffusion coefficient of standard water D and a diffusion coefficient of heavy isotope D'. The exponent m varies in the range 0–1 and represents the ratio of diffusive versus turbulent transport (see also Craig and Gordon 1965; Gat 1996; C03; Horita et al. 2008; PW09, and references therein). For $m = 0$ and $\alpha_k = 1$, the transport is purely turbulent, and no fractionation occurs. For $m = 1$, the transport is purely diffusive and nonequilibrium fractionation is important. Strongly diffusive conditions can be expected for very stagnant interfaces, as for example during soil evaporation, and have been observed in laboratory studies and in the field (Mathieu and Bariac 1996; Braud et al. 2009a,b; Aemisegger et al. 2014). Even though this formulation for α_k does not directly include a quantitative characterization of the laminar boundary layer and surface roughness (Noone et al. 2013), it is very tractable and can be easily related to different boundary layer structure and roughness parameters to determine the exponent m empirically under different turbulence conditions.

A simple and close to linear relationship between the comparatively easily measurable $d_c(h_s)$ slope [$s^{\mathrm{M78}}_{d_v(h_s)}$, using the Merlivat (1978) diffusivities] and the exponent m in the above α_k definition [Eq. (7)] can be obtained from the linearized CG65closure equation (see appendix C for the derivation):

$$m = -0.530\,45 s^{\mathrm{M78}}_{d_v(h_s)} - 0.006\,99. \tag{8}$$

In this study the exponent m was variable in the MJ79 parameterization: $m = 0.221$ for MJ79cstu6ms and $m = 0.28$ for PW09 (see PW09 for a more detailed discussion of the numerical value of m corresponding to their α_k). More measurements, ideally ship based, under different synoptic-scale conditions and particularly in the case of strong ocean evaporation during cold-air advection, including wind speed and surface roughness conditions, would provide valuable additional data to better constrain α_k.

Note, that a possible wind-dependent confounding factor for changes in the $d_c(h_s)$ slope is the deviation from closure conditions, particularly at high h_s. Then, the composition of the ambient background water vapor d_c feeds back onto d_e. Spatially distributed measurements including upstream and downstream conditions would thus be particularly useful.

4. Conclusions

In this paper we have presented global estimates of d_c during events of strong moisture uptake by the atmosphere resulting from strong large-scale ocean evaporation (SLOE) using different formulations of the nonequilibrium fractionation factor α_k. To compile this climatology, we have used the CG65closure model based on the closure assumption of MJ79 applied to the Craig and Gordon (1965) model formulation for water isotope evaporation. We showed that the closure assumption is more likely to be fulfilled for d during SLOE conditions for two reasons: 1) the large amount of fresh evaporate taken up by the dry airstreams inducing SLOE leads to a rapid overwriting of the background isotope composition, and 2) at low h_s that is characteristic of such events the influence of the background isotope composition is reduced compared to situations with high h_s.

For all the tested α_k parameterizations, we consistently find the highest d_c to occur along the warm WBCs in wintertime when SLOE is most frequent. Other regions with relatively high d_c values are found along the sea ice edge in the Norwegian Sea, the Labrador Sea, and the Ross Sea where cold-air outbreaks lead to strong near-surface humidity gradients. The spatial patterns of SLOE and cyclone d_c composites are similar, although the d_c values in the cyclone composites are approximately 10‰ lower, reflecting the importance of high h_s in cyclones particularly in areas of warm-air advection. The expected contrasts in the isotope composition of near-surface water vapor and evaporation d between warm- and cold-air advection areas in extratropical cyclones cannot however be investigated using the framework of this paper, because during warm-air advection the closure assumption is most likely not fulfilled (because of the high h_s, small humidity uptake, or even net humidity loss by the airstreams and the potential additional input of moisture by precipitation evaporation). More measurement data combined with isotope-enabled numerical model simulations are needed to investigate the differences in the boundary layer d signature under these two contrasting large-scale forcing situations. This will be possible with the extensive dataset of marine boundary layer water vapor isotope measurements gathered as part of the Antarctic Circumnavigation Expedition (ACE) in the Southern Ocean during December 2016–March 2017 (Swiss Polar Institute 2017).

In addition to the distinct high d_c anomaly associated with cold-air advection, we highlight the role of the cross correlation between h_s and SST as an important factor determining the properties of the d_c(SST) relation. Two regimes in the h_s–SST correlation have been described. In the positive feedback regime, the cross correlation between h_s and SST reinforces the direct CG65closure controls of h_s and SST on d_c. This regime is typically found in regions characterized by "warm ocean" SLOE

along the major warm WBCs. It reflects the classical interpretation of d_c as a positively related SST proxy and is generally assumed to be the dominating regime over long time scales. The negative feedback regime is associated with a weakening of the direct controls of h_s and SST on d_c. This second regime is more important at high latitudes for ''polar air'' and ''wind driven'' SLOE, particularly at synoptic–monthly time scales. This regime dominates in cases where the air temperature variability is large compared to the SST variability. An illustration of the negative feedback regime is given by the typical extratropical annual cycle in marine boundary layer d_c with higher SSTs during the summer along with high h_s, and lower SSTs along with low h_s during the winter.

By comparing wintertime d_c composites during SLOE for different α_k, we find similar spatial patterns but with a considerable spread in the absolute values, which emphasizes the need for measurement data to better constrain α_k. The wind dependency of the widely used MJ79 parameterization introduces a strong weakening of the d_c sensitivity to its primary control variables h_s and SST as well as unrealistic abrupt changes in the 6-hourly d_c fields as a result of the step change in the wind regime at $7\,\mathrm{m\,s^{-1}}$.

Globally, relatively constant $d_c(h_s)$ slopes of $-0.42‰\,\%^{-1}$ [α_k(MJ79cstu6ms)] and $-0.52‰\,\%^{-1}$ [α_k(PW09)] are found for the two-tested wind-independent α_k formulations, whereas a large spatial variability is introduced, when using the wind-dependent formulation α_k(MJ79).

Very large spatial variations are found in the d_c(SST) slopes for all tested α_k. This important spatial variability in the d_c(SST) sensitivities is linked to the spatially variable cross-correlation effects between h_s and SST.

An important aspect that should be further explored in the future is the possible imprint of the frequency of SLOE events on the d signals of Antarctic and Greenland ice cores. In this respect, the control of sea ice extent on the location of SLOE events, and the moisture sources associated with different drill sites becomes relevant. As shown by Steen-Larsen et al. (2013), high d in water vapor at the North Greenland Eemian Ice Drilling (NEEM) site is associated with air masses taking up water vapor near the sea ice margin. Furthermore, Noone and Simmonds (2004) investigated the d in interior Antarctica (water vapor and precipitation) in isotope-enabled model simulations and showed that d is strongly affected by the sea ice extent, although the study also underlines the discrepancy between modeled and measured d.

The findings in this study point out the important role of cold-air advection by extratropical cyclones in inducing distinct positive anomalies in the moisture source d_c. The fate of this high-d_c moisture taken up by cold air masses and its possible contribution to long-term d signals in precipitation and ice core data is a subject of future investigations. A possible link between high d anomalies in climate archives and moisture source SLOE activity would provide an important basis for understanding long-term variations of past changes in regional cold-air outbreak and extratropical cyclone activity.

Acknowledgments. FA acknowledges funding from the Swiss National Science Foundation (SNSF; Grant P2EZP2_155603). The research presented in this paper is a contribution to the Swedish strategic research area Modelling the Regional and Global Earth System (MERGE). MeteoSwiss and the ECMWF are acknowledged for providing access to the ERA-Interim data. This work was supported by a grant from the Swiss National Supercomputing Centre (CSCS) under projects s520 (2014–16) and sm08 (2017–19). We are grateful to Florian Adolphi (University of Bern and Lund University) for valuable discussions and Stephan Pfahl (Freie Universität Berlin) for his helpful comments on the manuscript. We thankfully acknowledge the valuable and insightful comments from three anonymous reviewers, who helped a lot in improving the clarity and focus of this paper.

APPENDIX A

Deviation from Closure during SLOE Compared to No-SLOE Conditions in a 3-Month $\mathrm{COSMO_{iso}}$ Simulation

The hypothesis that during SLOE events the strong moisture input into the atmosphere resulting from ocean evaporation leads to conditions that are close to closure (i.e., $d_v = d_e$) is tested using a 3-month wintertime simulation with $\mathrm{COSMO_{iso}}$ (Fig. A1). For details about the limited-area COSMO Model in general see Steppeler et al. (2003); for details about the water isotope implementation see Pfahl et al. (2012). The isotope implementation into the multilayer land surface scheme (TERRA; Schrodin and Heise 2001) is used as described in Dütsch (2016) and Christner et al. (2018). The simulation is performed over a large North Atlantic domain with a horizontal resolution of 0.25° and 6-hourly output. In this $\mathrm{COSMO_{iso}}$ simulation, the horizontal wind fields above 850 hPa are spectrally nudged (Von Storch et al. 2000) toward the reanalysis-based dynamical fields.

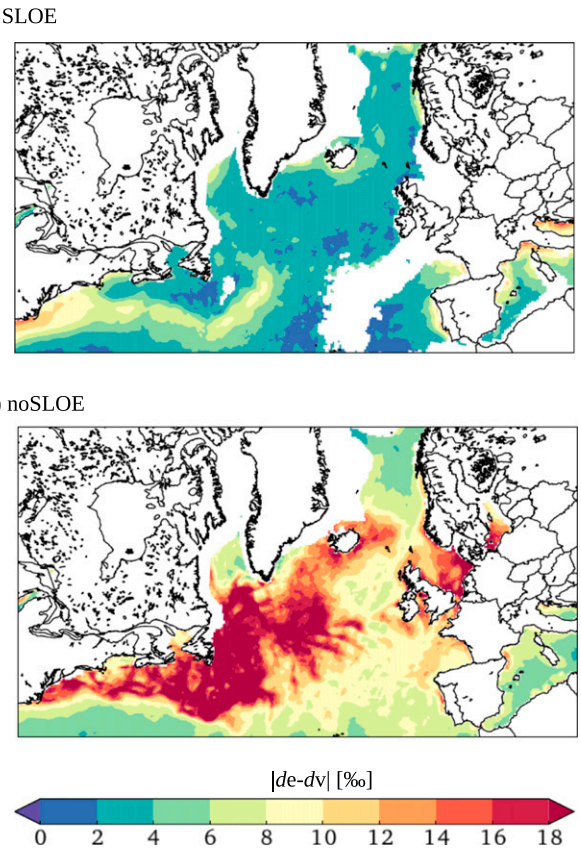

FIG. A1. Deviation from closure measured by the mean absolute difference between d_e and d_v during (a) SLOE and (b) no SLOE during a 3-month $\text{COSMO}_{\text{iso}}$ simulation. Regions with sea ice and occurrence frequencies of <5% for SLOE in (a) and no SLOE in (b), as well as land areas, are masked.

The initial and boundary conditions for all the non-isotopic model variables have been obtained from the ECMWF reanalysis data. For the isotope variables, data from the isoGCM (spectral T62 and 17 vertical levels) are used (Yoshimura et al. 2008). This dataset is produced by nudging the isoGCM toward global reanalysis data (Yoshimura et al. 2008). The non-equilibrium fractionation factor α_k(MJ79cstu6ms) is used. The results shown in Fig. A1 are similar when using other α_k definitions. The identification of SLOE events has been applied as described for the ERA-Interim dataset (Part I). Because of the different vertical model level definition (the first model layer has a depth of about 1.1 hPa and not around 2.4 hPa as in the ERA-Interim dataset) and the finer horizontal resolution, the identification parameters have been slightly modified. The moisture uptake efficiency threshold f_{evap} has been set to $5\,\text{h}^{-1}$.

The deviation from closure in the 3-month North Atlantic $\text{COSMO}_{\text{iso}}$ simulation is quantified by the absolute difference between the modeled d_e and d_v ($\Delta d_{e-v} = |d_e - d_v|$) for each grid point at each 6-hourly time step. For d_v the lowest model level is used. A composite mean of $\Delta d_{|e-v|}$ is computed for SLOE (Fig. A1a) and no-SLOE conditions (Fig. A1b). The $\Delta d_{|e-v|}$ composite during SLOE shows much smaller values than the $\Delta d_{|e-v|}$ composite during no SLOE. The spatial pattern of $\Delta d_{|e-v|}$ during SLOE highlights regions downstream of large continental areas such as along the Mediterranean Sea and the North Atlantic coasts of Europe and North America. These locally larger $\Delta d_{|e-v|}$ during SLOE are due to the advection of continental air with a distinct isotope signature. Comparatively larger values are also found along the Gulf Stream. A possible explanation for these larger deviations from closure along the storm track is the input of moisture into the boundary layer resulting from rainfall evaporation.

APPENDIX B

Comparison of Seasonal d_c from ERA-Interim for Different α_k with Measurements

For the years 2011–13 the obtained seasonal SLH-weighted mean d_c values were compared to the few year-around available water vapor isotope measurements from ocean-close setups (three stations in the North Atlantic and one station in eastern China; Table B1). The closest available ocean grid point was chosen to extract the seasonal means from the 1° horizontal resolution fields. The root-mean-square errors are between 5.6‰ and 7.4‰, which is in the range of the present uncertainties of the observations (~3‰–7‰ depending on the study). Given the fact that no transport effects are considered in our approach and that we use the closure assumption, the seasonal evaporation d_c compare relatively well with the measurement data. When using the wind-dependent α_k from MJ79, d_c is consistently underestimated compared to the measurements. This tendency is also present in studies comparing d_c from measurements with isotope-enabled numerical model simulations, which use the same α_k definition (Steen-Larsen et al. 2013; Risi et al. 2013; Bonne et al. 2014). Annual average d_c using the wind-independent α_k(PW09) have a consistent positive bias. Using α_k(MJ79cstu6ms) yields the best results although there is a tendency to underestimate d_c at the northern stations (Ivittuut and Iceland). This is probably due to the influence of transport and remote moisture sources affecting the measurements.

TABLE B1. Comparison of seasonal SLH-weighted means of d_c using the CG65closure model for different α_k (columns) with available measurements of at least 1 yr for the mentioned seasons. The d_c estimate from the different α_k that is closest to the observations is highlighted in italics. The root-mean-square difference (RMSD) between the seasonal mean d_c estimates and the measurements.

Study and season	Obs (‰)	MJ79 (‰)	PW09 (‰)	MJ79cstu6ms (‰)
Ivittuut (Bonne et al. 2014)				
DJF (Dec 2012 and Jan–Feb 2013)	15.9	9.6	19.2	*13.1* (*−2.8*)
MAM (Apr–May 2012 and Mar–May 2013)	11.8	5.7	*11.8* (*0*)	7.4
JJA 2012	8.7	−1.8	*0.0* (*−8.7*)	−1.3
SON (Oct–Nov 2011 and Nov 2012)	21.1	11.6	*18.1* (*−3.0*)	12.1
Iceland (Steen-Larsen et al. 2015)				
DJF (Dec 2011 and Jan–Feb 2012, and Dec 2012 and Jan–Feb 2013)	13.3	9.0	18.1	*12.6* (*−0.9*)
MAM 2012	16.4	9.6	*17.4* (*+1.0*)	12.1
JJA 2012	9	6.3	11.5	*8.0* (*−1.0*)
SON 2012	13.2	10.7	19.7	*14.1* (*+0.9*)
Bermuda (Steen-Larsen et al. 2014)				
DJF (Dec 2011 and Jan–Feb 2012, and Dec 2012 and Jan–Feb 2013)	17	13.7	22.43	*17.1* (*+0.1*)
JJA 2012	9	*9.0* (*0*)	13.9	11
Beijing (Wen et al. 2010)				
DJF (Dec 2006 and Jan–Feb 2007)	14.8	12.9	22.3	*15.5* (*+0.7*)
MAM 2007	14.1	8.3	*15.7* (*+1.6*)	10.9
JJA 2007	7.2	10.3	12.7	*9.9* (*+2.7*)
SON 2007	11.7	*18.2* (*+6.5*)	26.4	19.3
RMSD	—	6.8	7.4	5.6

APPENDIX C

Wind-Independent Formulation for α_k by CG65closure and Its Link with the $d_c(h_s)$ Slope

A simple and close to linear relationship between the $d_c(h_s)$ slope and the exponent m in the α_k definition [Eq. (7)] can be obtained from the linearized CG65closure equation. A Taylor expansion of Eq. (6) of the form

$$f(x) = f|_{h=0} + \left.\frac{df}{dh}\right|_{h=0} h + \text{higher-order terms} \tag{C1}$$

and neglecting higher-order terms leads to the following "linearized" CG65closure equation for d_c:

$$d_c(h_s) = \left[\frac{1000}{\alpha^{^2\mathrm{H}}\alpha_k^{^2\mathrm{H}}} - \frac{8000}{\alpha^{^{18}\mathrm{O}}\alpha_k^{^{18}\mathrm{O}}} + 7000\right] + \left[\frac{-1000\alpha^{^2\mathrm{H}}(1-\alpha_k^{^2\mathrm{H}})}{(\alpha^{^2\mathrm{H}}\alpha_k^{^2\mathrm{H}})^2} + \frac{8000\alpha^{^{18}\mathrm{O}}(1-\alpha_k^{^{18}\mathrm{O}})}{(\alpha^{^{18}\mathrm{O}}\alpha_k^{^{18}\mathrm{O}})^2}\right] h_s. \tag{C2}$$

This simple expression can be of practical use as it allows us to explicitly link the stability-dependent exponent m to measurable physical parameters that are commonly assumed to control the evaporation of water isotopes such as d_c, h_s, and SST, as well as the relatively well-known diffusivities of the water molecules. The validity of this expression is however restricted to strongly evaporative conditions that justify

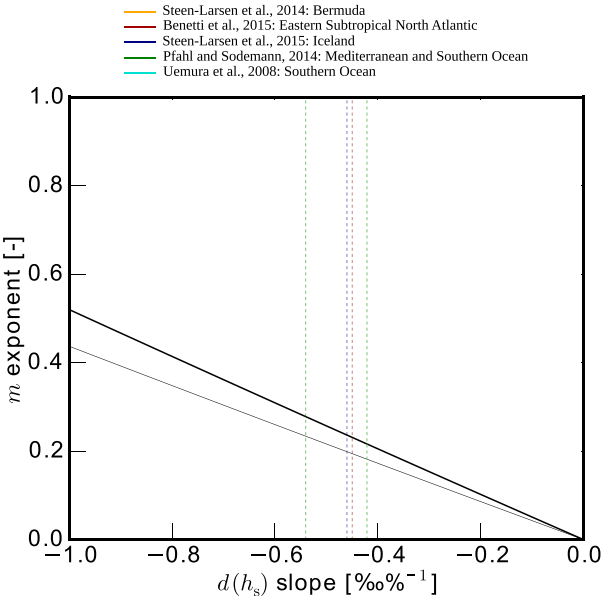

FIG. C1. The exponent m in the wind-independent CG65closure formulation of α_k as a function of $d_c(h_s)$ slopes. The thick black line is the resulting relationship when using diffusivities of Merlivat (1978) and the thin black line when using the diffusivities of C03.

the use of the closure assumption. The resulting close to linear relationship between the exponent m and the d_c (h_s) slope is shown in Fig. C1.

REFERENCES

Aemisegger, F., and L. Papritz, 2018: A climatological analysis of strong large-scale ocean evaporation. Part I: Identification, global distribution, and associated climate conditions. *J. Climate*, **31**, 7287–7312, https://doi.org/10.1175/JCLI-D-17-0591.1.

——, P. Sturm, P. Graf, H. Sodemann, S. Pfahl, A. Knohl, and H. Wernli, 2012: Measuring variations of δ^{18}O and δ^{2}H in atmospheric water vapour using two commercial laser-based spectrometers: An instrument characterisation study. *Atmos. Meas. Tech.*, **5**, 1491–1511, https://doi.org/10.5194/amt-5-1491-2012.

——, S. Pfahl, H. Sodemann, I. Lehner, S. I. Seneviratne, and H. Wernli, 2014: Deuterium excess as a proxy for continental moisture recycling and plant transpiration. *Atmos. Chem. Phys.*, **14**, 4029–4054, https://doi.org/10.5194/acp-14-4029-2014.

Angert, A., J.-E. Lee, and D. Yakir, 2008: Seasonal variations in the isotopic composition of near-surface water vapour in the eastern Mediterranean. *Tellus*, **60B**, 674–684, https://doi.org/10.1111/j.1600-0889.2008.00357.x.

Araguás-Araguás, L., K. Froehlich, and K. Rozanski, 2000: Deuterium and oxygen-18 isotope composition of precipitation and atmospheric moisture. *Hydrol. Processes*, **14**, 1341–1355, https://doi.org/10.1002/1099-1085(20000615)14:8<1341::AID-HYP983>3.0.CO;2-Z.

Bailey, A., D. Noone, M. Berkelhammer, H. C. Steen-Larsen, and P. Sato, 2015: The stability and calibration of water vapor isotope ratio measurements during long-term deployments. *Atmos. Meas. Tech.*, **8**, 4521–4538, https://doi.org/10.5194/amt-8-4521-2015.

Benetti, M., G. Reverdin, C. Pierre, L. Merlivat, C. Risi, H. C. Steen-Larsen, and F. Vimeux, 2014: Deuterium excess in marine water vapor: Dependency on relative humidity and surface wind speed during evaporation. *J. Geophys. Res. Atmos.*, **119**, 584–593, https://doi.org/10.1002/2013JD020535.

Bonne, J.-L., V. Masson-Delmotte, O. Cattani, M. Delmotte, C. Risi, H. Sodemann, and H. C. Steen-Larsen, 2014: The isotopic composition of water vapour and precipitation in Ivittuut, southern Greenland. *Atmos. Chem. Phys.*, **14**, 4419–4439, https://doi.org/10.5194/acp-14-4419-2014.

Braud, I., P. Biron, T. Bariac, P. Richard, L. Canale, J. Gaudet, and M. Vauclin, 2009a: Isotopic composition of bare soil evaporated water vapor. Part I: RUBIC IV experimental set up and results. *J. Hydrol.*, **369**, 1–16, https://doi.org/10.1016/j.jhydrol.2009.01.034.

——, T. Bariac, P. Biron, and M. Vauclin, 2009b: Isotopic composition of bare soil evaporated water vapor. Part II: Modeling of RUBIC IV experimental results. *J. Hydrol.*, **369**, 17–29, https://doi.org/10.1016/j.jhydrol.2009.01.038.

Brown, J., and I. Simmonds, 2004: Sensitivity of the δ^{18}O-temperature relationship to the distribution of continents. *Geophys. Res. Lett.*, **31**, L09208, https://doi.org/10.1029/2004GL019870.

Brutsaert, W., 1975: A theory for local evaporation (or heat transfer) from rough and smooth surfaces at ground level. *Water Resour. Res.*, **11**, 543–550, https://doi.org/10.1029/WR011i004p00543.

Cappa, C. D., M. B. Hendricks, D. J. DePaolo, and R. C. Cohen, 2003: Isotopic fractionation of water during evaporation. *J. Geophys. Res.*, **108**, 4525, https://doi.org/10.1029/2003JD003597.

Christner, E., and Coauthors, 2018: The climatological impacts of continental surface evaporation, rainout, and sub-cloud processes on δD of water vapour and precipitation in Europe. *J. Geophys. Res. Atmos.*, **123**, 4390–4409, https://doi.org/10.1002/2017JD027260.

Ciais, P., and J. Jouzel, 1994: Deuterium and oxygen 18 in precipitation: Isotopic model, including mixed cloud processes. *J. Geophys. Res.*, **99**, 16 793–16 803, https://doi.org/10.1029/94JD00412.

Coplen, T. B., 2011: Guidelines and recommended terms for expression of stable-isotope-ratio and gas-ratio measurement results. *Rapid Commun. Mass Spectrom.*, **25**, 2538–2560, https://doi.org/10.1002/rcm.5129.

Craig, H., and L. Gordon, 1965: Deuterium and oxygen 18 variations in the ocean and the marine atmosphere. *Stable Isotopes in Oceanographic Studies and Paleotemperatures*, E. Tongiorgi, Eds., Laboratorio di Geologia Nucleare, 9–130.

Dansgaard, W., 1964: Stable isotopes in precipitation. *Tellus*, **16**, 436–468, https://doi.org/10.3402/tellusa.v16i4.8993.

Dee, D. P., and Coauthors, 2011: The ERA-Interim reanalysis: Configuration and performance of the data assimilation system. *Quart. J. Roy. Meteor. Soc.*, **137**, 553–597, https://doi.org/10.1002/qj.828.

Delaygue, G., V. Masson, J. Jouzel, R. D. Koster, and R. J. Healy, 2000: The origin of Antarctic precipitation: A modelling approach. *Tellus*, **52B**, 19–36, https://doi.org/10.3402/tellusb.v52i1.16079.

Dütsch, M., 2016: Stable water isotope fractionation processes in weather systems and their influence on isotopic variability on different time scales. Ph.D. Dissertation 23939, ETH Zurich, Zurich, Switzerland, 159 pp., https://www.research-collection.ethz.ch/handle/20.500.11850/58.

——, S. Pfahl, and H. Sodemann, 2017: The impact of rainout and mixing on two different deuterium excess definitions. *J. Geophys. Res. Atmos.*, **122**, 12 732–12 746, https://doi.org/10.1002/2017JD027085.

Eriksson, E., and B. Bolin, 1964: Oxygen-18, deuterium and tritium in natural waters and their relations to the global circulation of water. *Radioactive Fallout from Nuclear Weapon Tests*, A. W. Klement, Ed., U.S. Atomic Energy Commission, 675–686.

Gat, J. R., 1996: Oxygen and hydrogen isotopes in the hydrologic cycle. *Annu. Rev. Earth Planet. Sci.*, **24**, 225–262, https://doi.org/10.1146/annurev.earth.24.1.225.

——, B. Klein, Y. Kushnir, W. Roether, H. Wernli, R. Yam, and A. Shemesh, 2003: Isotope composition of air moisture over the Mediterranean Sea: An index of the air–sea interaction pattern. *Tellus*, **55B**, 953–965, https://doi.org/10.1034/j.1600-0889.2003.00081.x.

Horita, J., and D. J. Wesolowski, 1994: Liquid-vapor fractionation of oxygen and hydrogen isotopes of water from the freezing to the critical temperature. *Geochim. Cosmochim. Acta*, **58**, 3425–3437, https://doi.org/10.1016/0016-7037(94)90096-5.

——, K. Rozanski, and S. Cohen, 2008: Isotope effects in the evaporation of water: A status report of the Craig–Gordon model. *Isotopes Environ. Health Stud.*, **44**, 23–49, https://doi.org/10.1080/10256010801887174.

IAEA/WMO, 2018: Global Network of Isotopes in Precipitation. The GNIP database. Int. Atomic Energy Agency, http://www.iaea.org/water.

Johnsen, S. J., W. Dansgaard, and J. W. C. White, 1989: The origin of Arctic precipitation under present and glacial conditions. *Tellus*, **41B**, 452–468, https://doi.org/10.1111/j.1600-0889.1989.tb00321.x.

Jouzel, J., and R. D. Koster, 1996: A reconsideration of the initial conditions used for stable water isotope models. *J. Geophys. Res.*, **101**, 22 933–22 938, https://doi.org/10.1029/96JD02362.

——, L. Merlivat, and C. Lorius, 1982: Deuterium excess in an East Antarctic ice core suggests higher relative humidity at the oceanic surface during the last glacial maximum. *Nature*, **299**, 688–691, https://doi.org/10.1038/299688a0.

——, and Coauthors, 2007a: Orbital and millennial Antarctic climate variability over the past 800,000 years. *Science*, **317**, 793–796, https://doi.org/10.1126/science.1141038.

——, and Coauthors, 2007b: The GRIP deuterium-excess record. *Quat. Sci. Rev.*, **26**, 1–17, https://doi.org/10.1016/j.quascirev.2006.07.015.

Kurita, N., 2011: Origin of Arctic water vapor during the ice-growth season. *Geophys. Res. Lett.*, **38**, L02709, https://doi.org/10.1029/2010GL046064.

——, N. Hirasawa, S. Koga, J. Matsushita, H. C. Steen-Larsen, V. Masson-Delmotte, and Y. Fujiyoshi, 2016: Influence of large-scale atmospheric circulation on marine air intrusion toward the East Antarctic coast. *Geophys. Res. Lett.*, **43**, 9298–9305, https://doi.org/10.1002/2016GL070246.

Majoube, M., 1971: Fractionnement en oxygene 18 et en deuterium entre l'eau et sa vapeur. *J. Chim. Phys.*, **68**, 1423–1436, https://doi.org/10.1051/jcp/1971681423.

Markle, B. R., and Coauthors, 2017: Global atmospheric teleconnections during Dansgaard–Oeschger events. *Nat. Geosci.*, **10**, 36–40, https://doi.org/10.1038/ngeo2848.

Masson-Delmotte, V., and Coauthors, 2005: GRIP deuterium excess reveals rapid and orbital-scale changes in Greenland moisture origin. *Science*, **309**, 118–121, https://doi.org/10.1126/science.1108575.

Mathieu, R., and T. Bariac, 1996: A numerical model for the simulation of stable isotope profiles in drying soils. *J. Geophys. Res.*, **101**, 12 685–12 696, https://doi.org/10.1029/96JD00223.

Merlivat, L., 1978: The dependence of bulk evaporation coefficients on air-water interfacial conditions as determined by the isotopic method. *J. Geophys. Res.*, **83**, 2977–2980, https://doi.org/10.1029/JC083iC06p02977.

——, and J. Jouzel, 1979: Global climatic interpretation of the deuterium-oxygen 18 relationship for precipitation. *J. Geophys. Res.*, **84**, 5029–5033, https://doi.org/10.1029/JC084iC08p05029.

Noone, D., and I. Simmonds, 2002: Annular variations in moisture transport mechanisms and the abundance of δ^{18}O in Antarctic snow. *J. Geophys. Res.*, **107**, 4742, https://doi.org/10.1029/2002JD002262.

——, and ——, 2004: Sea ice control of water isotope transport to Antarctica and implications for ice core interpretation. *J. Geophys. Res.*, **109**, D07105, https://doi.org/10.1029/2003JD004228.

——, and Coauthors, 2013: Determining water sources in the boundary layer from tall tower profiles of water vapor and surface water isotope ratios after a snowstorm in Colorado. *Atmos. Chem. Phys.*, **13**, 1607–1623, https://doi.org/10.5194/acp-13-1607-2013.

Pasquill, F., 1943: Evaporation from a plane, free-liquid surface into a turbulent air stream. *Proc. Roy. Soc. London*, **182A**, 75–94, https://doi.org/10.1098/rspa.1943.0024.

Petit, J. R., J. W. C. White, N. W. Young, J. Jouzel, and Y. S. Korotkevich, 1991: Deuterium excess in recent Antarctic snow. *J. Geophys. Res.*, **96**, 5113–5122, https://doi.org/10.1029/90JD02232.

Pfahl, S., and H. Wernli, 2008: Air parcel trajectory analysis of stable isotopes in water vapor in the eastern Mediterranean. *J. Geophys. Res.*, **113**, D20104, https://doi.org/10.1029/2008JD009839.

——, and ——, 2009: Lagrangian simulations of stable isotopes in water vapor: An evaluation of nonequilibrium fractionation in the Craig–Gordon model. *J. Geophys. Res.*, **114**, D20108, https://doi.org/10.1029/2009JD012054.

——, and H. Sodemann, 2014: What controls deuterium excess in global precipitation? *Climate Past*, **10**, 771–781, https://doi.org/10.5194/cp-10-771-2014.

——, H. Wernli, and K. Yoshimura, 2012: The isotopic composition of precipitation from a winter storm – A case study with the limited-area model COSMOiso. *Atmos. Chem. Phys.*, **12**, 1629–1648, https://doi.org/10.5194/acp-12-1629-2012.

Risi, C., A. Landais, R. Winkler, and F. Vimeux, 2013: Can we determine what controls the spatio-temporal distribution of d-excess and ^{17}O-excess in precipitation using the LMDZ general circulation model? *Climate Past*, **9**, 2173–2193, https://doi.org/10.5194/cp-9-2173-2013.

Rudeva, I., and I. Simmonds, 2015: Variability and trends of global atmospheric frontal activity and links with large-scale modes of variability. *J. Climate*, **28**, 3311–3330, https://doi.org/10.1175/JCLI-D-14-00458.1.

Schneider, T., P. A. O'Gorman, and X. J. Levine, 2010: Water vapor and the dynamics of climate changes. *Rev. Geophys.*, **48**, RG3001, https://doi.org/10.1029/2009RG000302.

Schrodin, R., and E. Heise, 2001: The multi-layer version of the DWD soil model TERRA_LM. COSMO Tech. Rep. 2, Deutscher Wetterdienst, Offenbach am Main, Germany, 16 pp., http://www.cosmo-model.org/content/model/documentation/techReports/docs/techReport02.pdf.

Shaw, T. A., and Coauthors, 2016: Storm track processes and the opposing influences of climate change. *Nat. Geosci.*, **9**, 656–665, https://doi.org/10.1038/ngeo2783.

Sodemann, H., and A. Stohl, 2009: Asymmetries in the moisture origin of Antarctic precipitation. *Geophys. Res. Lett.*, **36**, L22803, https://doi.org/10.1029/2009GL040242.

——, C. Schwierz, and H. Wernli, 2008a: Interannual variability of Greenland winter precipitation sources: Lagrangian moisture diagnostic and North Atlantic Oscillation influence. *J. Geophys. Res.*, **113**, D03107, https://doi.org/10.1029/2007JD008503.

——, V. Masson-Delmotte, C. Schwierz, B. M. Vinther, and H. Wernli, 2008b: Interannual variability of Greenland winter precipitation sources: 2. Effects of North Atlantic Oscillation variability on stable isotopes in precipitation. *J. Geophys. Res.*, **113**, D12111, https://doi.org/10.1029/2007JD009416.

——, and Coauthors, 2017: The stable isotopic composition of water vapour above Corsica during the HyMeX SOP1 campaign: Insight into vertical mixing processes from lower-tropospheric survey flights. *Atmos. Chem. Phys.*, **17**, 6125–6151, https://doi.org/10.5194/acp-17-6125-2017.

Sprenger, M., and Coauthors, 2017: Global climatologies of Eulerian and Lagrangian flow features based on ERA-Interim. *Bull. Amer. Meteor. Soc.*, **98**, 1739–1748, https://doi.org/10.1175/BAMS-D-15-00299.1.

Steen-Larsen, H. C., and Coauthors, 2013: Continuous monitoring of summer surface water vapor isotopic composition above the Greenland Ice Sheet. *Atmos. Chem. Phys.*, **13**, 4815–4828, https://doi.org/10.5194/acp-13-4815-2013.

——, and Coauthors, 2014: Climatic controls on water vapor deuterium excess in the marine boundary layer of the North Atlantic based on 500 days of in situ, continuous measurements. *Atmos. Chem. Phys.*, **14**, 7741–7756, https://doi.org/10.5194/acp-14-7741-2014.

——, and Coauthors, 2015: Moisture sources and synoptic to seasonal variability of North Atlantic water vapor isotopic composition. *J. Geophys. Res. Atmos.*, **120**, 5757–5774, https://doi.org/10.1002/2015JD023234.

——, C. Risi, M. Werner, K. Yoshimura, and V. Masson-Delmotte, 2017: Evaluating the skills of isotope-enabled general circulation models against in situ atmospheric water vapor isotope observations. *J. Geophys. Res. Atmos.*, **122**, 246–263, https://doi.org/10.1002/2016JD025443.

Steffensen, J. P., and Coauthors, 2008: High-resolution Greenland ice core data show abrupt climate change happens in few years. *Science*, **321**, 680–684, https://doi.org/10.1126/science.1157707.

Stenni, B., V. Masson-Delmotte, S. Johnsen, J. Jouzel, A. Longinelli, E. Monnin, R. Röthlisberger, and E. Selmo, 2001: An oceanic cold reversal during the last deglaciation. *Science*, **293**, 2074–2077, https://doi.org/10.1126/science.1059702.

Steppeler, J., G. Doms, U. Schättler, H. W. Bitzer, A. Gassmann, U. Damrath, and G. Gregoric, 2003: Meso-gamma scale forecasts using the nonhydrostatic model LM. *Meteor. Atmos. Phys.*, **82**, 75–96, https://doi.org/10.1007/s00703-001-0592-9.

Sutton, O. G., 1934: Wind structure and evaporation in a turbulent atmosphere. *Proc. Roy. Soc. London*, **146A**, 701–722, https://doi.org/10.1098/rspa.1934.0183.

Swiss Polar Institute, 2017: Antarctic Circumnavigation Expedition. http://spi-ace-expedition.ch/.

Tanny, J., and J. Cohen, 2008: Revisiting the boundary layer structure used in Craig and Gordon's model of isotope fractionation in evaporation. *Isotopes Environ. Health Stud.*, **44**, 11–21, https://doi.org/10.1080/10256010801887091.

Uemura, R., Y. Matsui, K. Yoshimura, H. Motoyama, and N. Yoshida, 2008: Evidence of deuterium excess in water vapor as an indicator of ocean surface conditions. *J. Geophys. Res.*, **113**, D19114, https://doi.org/10.1029/2008JD010209.

Vimeux, F., V. Masson, J. Jouzel, M. Stievenard, and J. R. Petit, 1999: Glacial–interglacial changes in ocean surface conditions in the Southern Hemisphere. *Nature*, **398**, 410–413, https://doi.org/10.1038/18860.

Von Storch, H., H. Langenberg, and F. Feser, 2000: A spectral nudging technique for dynamical downscaling purposes. *Mon. Wea. Rev.*, **128**, 3664–3673, https://doi.org/10.1175/1520-0493(2000)128<3664:ASNTFD>2.0.CO;2.

Welp, L. R., and Coauthors, 2012: A meta-analysis of water vapor deuterium-excess in the midlatitude atmospheric surface layer. *Global Biogeochem. Cycles*, **26**, GB3021, https://doi.org/10.1029/2011GB004246.

Wen, X.-F., S.-C. Zhang, X.-M. Sun, G.-R. Yu, and X. Lee, 2010: Water vapor and precipitation isotope ratios in Beijing, China. *J. Geophys. Res.*, **115**, D01103, https://doi.org/10.1029/2009JD012408.

Werner, M., M. Heimann, and G. Hoffmann, 2001: Isotopic composition and origin of polar precipitation in present and glacial climate simulations. *Tellus*, **53B**, 53–71, https://doi.org/10.3402/tellusb.v53i1.16539.

Wernli, H., and C. Schwierz, 2006: Surface cyclones in the ERA-40 dataset (1958–2001). Part I: Novel identification method and global climatology. *J. Atmos. Sci.*, **63**, 2486–2507, https://doi.org/10.1175/JAS3766.1.

Yoshimura, K., M. Kanamitsu, D. Noone, and T. Oki, 2008: Historical isotope simulation using Reanalysis atmospheric data. *J. Geophys. Res.*, **113**, D19108, https://doi.org/10.1029/2008JD010074.